

# Technical Memorandum



**Date:** April 17, 2019  
**To:** PFC 6.0 Documentation Set  
**From:** David Potyondy  
**Re:** Pavement-Design Package for PFC3D [pdPkg6.1]  
**Ref:** ICG16-8528-15TM

---

**April 1, 2019.** The pdPkg6.1 is for PFC3D version 6.0 and provides the same capabilities as pdPkg15. pdPkg15 is the complete final pdPkg for PFC3D version 5.

---

This memo describes the pavement-design package for the Particle Flow Code in 3 Dimensions (*PFC3D*, Itasca [2019]).<sup>1</sup> The package supports creation and triaxial testing of a synthetic unsaturated granular material containing geogrid (see Figure 3).<sup>2</sup> The geogrid provides lateral restraint to the granular material as a result of interlocking and friction between the geogrid and the granular material, and this is believed to be the primary structural benefit of adding geogrid to the aggregate base layer of a pavement structure. The package can be used to study and quantify the effect of microstructural properties on macroscopic response, which includes the stress-strain curves produced during triaxial tests. The microstructural properties of the granular material include: grain size distribution of spherical or clumped grains, grain material type, moisture content and initial specimen porosity. The microstructural properties of the geogrid include: geometry, structural stiffness and grid-surface behavior. The package is being used to improve pavement-design methodology in Minnesota by estimating geogrid gain factors (defined as the ratio of resilient modulus of the aggregate base with geogrid to resilient modulus of the aggregate base without geogrid) for typical geogrid-reinforced aggregate roadway configurations in which the grain-size distribution, initial specimen porosity, moisture content and confining stress are varied (Potyondy et al., 2016; Siekmeier et al., 2016; Siekmeier and Casanova, 2016). The package could be extended to investigate the behavior of other aggregate-geogrid systems such as a geogrid pull-out or wheel-load test.

---

<sup>1</sup> The pavement-design package is provided in the form of a consistent set of FISH functions that operate within *PFC3D* version 6.0. FISH is a programming language embedded within *PFC3D*. The *PFC3D* code can be obtained from <http://www.itascacg.com/pfc>, and the pavement-design package can be obtained from <http://www.itascacg.com/pavement-design-package>.

<sup>2</sup> The package also supports Dynamic Cone Penetrometer (DCP) and Light Weight Deflectometer (LWD) tests on the synthetic material (Potyondy, 2018).

Pavement-design methodology is summarized in the first major section. The pavement-design package is described in the second major section, with an emphasis on the geogrid-modeling methodology. Pavement-design examples are given in the third major section. A typical aggregate base layer of an asphalt-surface roadway is modeled. The resilient modulus is measured, for dry and wet conditions both with and without a geogrid, by performing triaxial tests on the modeled systems.

---

## TABLE OF CONTENTS

1.0	PAVEMENT-DESIGN METHODOLOGY .....	4
1.1	Layered Elastic Analysis .....	4
1.2	Geogrid Gain Factor .....	6
1.3	Unsaturated Condition of Pavement Materials .....	7
2.0	PAVEMENT-DESIGN PACKAGE .....	8
2.1	Grid-Modeling Methodology: Grid Set .....	9
2.1.1	Parallel-bonded grid .....	14
2.1.2	Beamed grid .....	18
2.2	Grid Calibration: Single Rib Tensile Tests .....	20
2.2.1	Parallel-bonded grid (biaxial) .....	23
2.2.2	Beamed grid (biaxial) .....	24
2.2.3	Beamed grid (triaxial) .....	25
2.3	Grid Calibration: Aperture Stability Modulus Tests .....	26
2.3.1	Parallel-bonded grid (biaxial) .....	29
2.3.2	Beamed grid (biaxial) .....	31
2.3.3	Beamed grid (triaxial) .....	32
2.4	Grid Calibration: Multiple Aperture Tensile Tests .....	33
2.4.1	Parallel-bonded grid (biaxial) .....	34
2.4.2	Beamed grid (biaxial) .....	35
2.4.3	Beamed grid (triaxial) .....	37
2.5	Grid-Embedment Procedure .....	38
3.0	PAVEMENT-DESIGN EXAMPLES .....	41
3.1	Simple Example .....	41
3.2	Realistic Example .....	50
4.0	REFERENCES .....	55

## 1.0 PAVEMENT-DESIGN METHODOLOGY

The first subsection outlines the layered elastic analysis that is used to support pavement design via *MnPAVE* (Tanquist, 2012). The second subsection introduces the geogrid gain factor as a means to modify the *MnPAVE* design modulus to account for the presence of geogrid within the aggregate base layer. And the final subsection discusses the unsaturated condition of pavement materials.

### 1.1 Layered Elastic Analysis

The mechanistic-empirical flexible pavement design program *MnPAVE* embodies an accepted procedure for the design of flexible pavements in Minnesota. *MnPAVE* simulates traffic loads on a pavement using a layered elastic analysis (LEA). The LEA is an axisymmetric, isotropic, elastic-layer model with bottom and sides at infinity, wheel load at the top, parameterized by thickness, Young's modulus and Poisson's ratio for each of the five layers, and allowing full to zero slip interface conditions. *MnPAVE* enforces the zero-slip condition to compute normal and shear stress, normal strain and displacement within the system shown in Figure 1. Of particular importance is the horizontal tensile strain at the bottom of the asphalt layer ( $\epsilon_h$ ), and the vertical compressive strain at the top of the compacted soil layer ( $\epsilon_v$ ). An excessive value of  $\epsilon_h$  can result in a fatigue crack forming and continuing upwards to the pavement surface, and an excessive vertical stress associated with  $\epsilon_v$  can result in permanent deformation in the compacted soil layer, which over time will be visible at the pavement surface as rutting. Estimates of fatigue and rutting life are obtained via empirical relations that employ these quantities ( $\epsilon_h$  for fatigue and  $\epsilon_v$  for rutting). Both life estimates must be greater than twenty years for the design to be acceptable. The inputs to *MnPAVE* include the thickness and material type of each layer, climate and traffic. The parameters are tied to one another via empirical relations. For example, life predictions require integrating the damage effects of wheel loading over time, and the climate dictates moisture conditions, which affect the elastic constants.



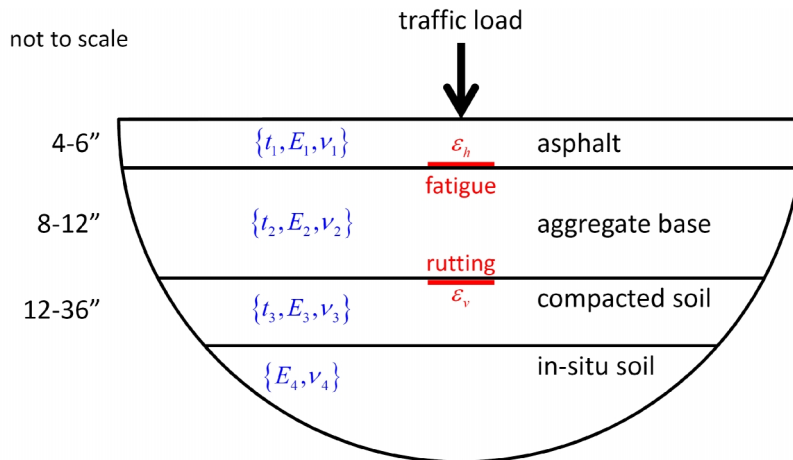


**Figure 1** Layered elastic analysis showing inputs (blue), typical layer names and thicknesses, and outputs (red) used to estimate fatigue and rutting life of flexible pavements.

Traffic loading in pavement analysis is conventionally simplified as a cyclic deviator stress ( $\sigma_d$ ). The repeated application of the deviator stress results in permanent strain ( $\epsilon_p$ ) and resilient strain ( $\epsilon_r$ ) within pavement materials, as shown in Figure 2. The resilient modulus ( $M_R$ ) is defined as the ratio of applied deviator stress to recoverable or “resilient” strain. It is a granular material characterization parameter that is stress dependent. The resilient modulus is used as the design modulus for the layered elastic analysis shown in Figure 1. LEA is utilized extensively for pavement system evaluation and is a means of calculating pavement response under loading. Each pavement layer is defined by its resilient modulus and Poisson’s ratio, even though granular bases exhibit nonlinear elastoplastic behavior in laboratory and field applications. LEA is used because it is a relatively simple analysis procedure and, more importantly, pavement loading is generally of low enough magnitude that a linear-elastic approximation of pavement material behavior is deemed suitable. According to Han and Vanapalli (2016), the resilient modulus is “...the key soil property in the mechanistic pavement design methods to rationally characterize the resilient behavior of the pavement materials, analyze the fatigue failure of the surface layer, and dimension the multi-layer system of the pavement structure.”

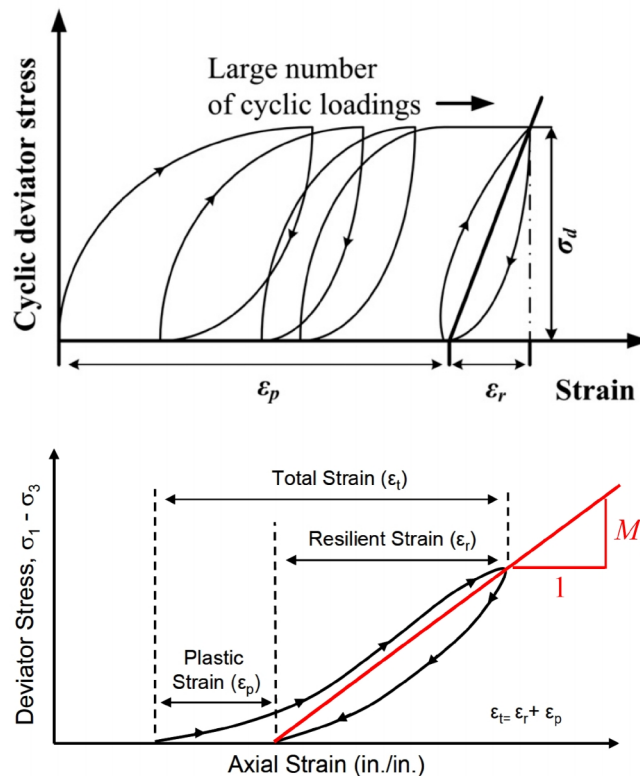


**Figure 2** *Response of granular material to cyclic deviator stress (top), and measurement of resilient modulus (bottom).* (From Fig. 2 of Han and Vanapalli [2016], and Fig. 1 of Buchanan [2007].)

## 1.2 Geogrid Gain Factor

The material in this subsection is a summary of the more extensive presentation in Potyondy et al. (2016). The traditional reason to use geogrid in Minnesota has been to provide a more stable construction platform by improving the strength of the pavement foundation when weak soils are present (Clyne, 2001). A more recent reason to use geogrid has been to provide additional stiffness to the aggregate base layer. Geogrid use is known to increase aggregate compaction during construction, thereby allowing the aggregate base to more effectively protect the underlying soil layers from traffic loads. Geogrid use is also expected to improve both the short- and long-term performance of roadways; however, greater justification and quantification of this expectation is desired.

The primary structural benefit of adding geogrid to the aggregate base layer of a flexible pavement is to provide lateral restraint. Lateral restraint is provided for the base layer as the result of interlocking and friction between the geogrid and the aggregate. Under repeated loads, the base layer tends to spread laterally, and some of the shear stress in the base layer can be transferred to tensile stress in the geogrid. A stiff geogrid will act to restrain the lateral spreading and result in a stiffer aggregate base. The lateral-restraint mechanism (as summarized in Bagshaw et al. [2015]) “. . . is that by

restricting the ability of the aggregate particles to move, and by effectively fixing them into place via interaction with the geogrid, mass transfer through the pavement will be restricted. If particles cannot move, then the modulus of the matrix will be maintained, and the rate of accumulation of plastic deformation via shear and/or consolidation will be reduced.”

It is understood that the use of geogrids in roadway aggregate base layer construction is beneficial (Skallman, 2010); however, *MnPAVE* does not account for the presence of a geogrid within the aggregate base layer. The geogrid gain factor is introduced as a means to modify the *MnPAVE* design modulus to account for the presence of geogrid within the aggregate base layer. The geogrid gain factor is defined as the ratio of resilient modulus of the aggregate base with geogrid to resilient modulus of the aggregate base without geogrid. The pavement-design package is used to estimate the geogrid gain factors for typical aggregate-geogrid roadway configurations (Siekmeier et al, 2016). Triaxial tests of an aggregate base, both with and without geogrid, are modeled, and the resilient moduli are measured in these tests to estimate the geogrid gain factor. The *MnPAVE* design modulus for the aggregate base with geogrid is found by multiplying the design modulus for the aggregate base without geogrid by the gain factor.

### 1.3 Unsaturated Condition of Pavement Materials

Han and Vanapalli (2016) describe the unsaturated condition of pavement materials, and argue for the use of soil suction to predict their mechanical behavior.

Compacted pavement base/subbase materials and subgrade soils stay in an unsaturated condition and are subjected to environmental influences. Environmental factors contribute to moisture regime and soil suction ( $\psi$ ) variations within the pavement structure which, in turn, influence strength and stiffness of pavement materials. Several research studies in recent years have demonstrated the strong correlations between the mechanical properties of unsaturated soils and the  $\psi$ . It is therefore recommended to use  $\psi$  as a key parameter to interpret and predict the response of the mechanical behavior of unsaturated soils to the soil moisture regime fluctuations. (Han and Vanapalli, 2016, p. 1)

The pavement-design package provides a means to predict the  $M_R - \psi$  correlations for typical pavement materials both with and without geogrid.

## 2.0 PAVEMENT-DESIGN PACKAGE

The pavement-design package supports creation and triaxial testing of a synthetic unsaturated granular material containing geogrid (see Figure 3). The mechanical behavior of this discrete system is simulated by the three-dimensional discrete-element program *PFC3D*. The model can simulate the movement and interaction of hundreds of thousands of finite-sized particles. The particles are rigid bodies with finite mass that move independently of one another and can both translate and rotate. Particles interact at pair-wise contacts by means of an internal force and moment. Contact mechanics is embodied in particle-interaction laws (called contact models) that update the internal forces and moments. The time evolution of this system is computed via the distinct-element method, which provides an explicit dynamic solution to Newton's laws of motion. The PFC model can be envisioned as a synthetic material that encompasses a vast microstructural space spanning from the granular material described here to the rich variety of solid materials provided by the bonded-particle modeling methodology (Potyondy, 2015). The synthetic system described here consists of unsaturated granular material and geogrid. The unsaturated granular material is modeled as spherical or clumped grains that interact with one another via the hill contact model. The synthetic material is denoted as a hill material and described in Potyondy (2019c). The geogrid is modeled as strings of overlapping spherical balls joined by either parallel bonds or beamed contacts. The parallel bonds or beamed contacts provide the structural properties of the grid, and the spherical balls provide the surface for grid-object interaction.

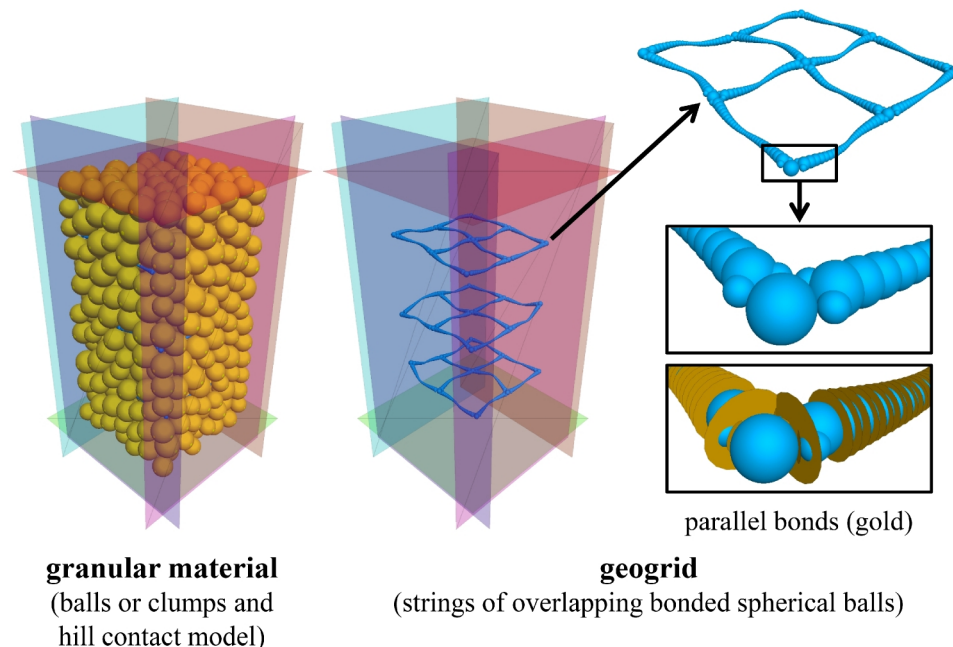


**Figure 3** *Pavement-design package supports creation and triaxial testing of synthetic unsaturated granular material containing geogrid, and measurement of resilient modulus for grid and no grid.*

The grid-modeling methodology is described in the first subsection. The geogrids are specified as a grid set consisting of identical flat geogrids oriented perpendicular to the specimen axis and spaced evenly in the axial direction (see Figure 4). The grid-set description includes a definition of the grid-set parameters as well as the closed-form expressions defining the sizes and locations of the balls and either the radii of the parallel bonds for the parallel-bonded grid or the width and height of the rib cross section for the beamed grid. The grid-set properties are chosen to match the geogrid geometry, the rib tensile stiffness from a Single Rib Tensile test, and the junction torsional stiffness from an Aperture Stability Modulus test. These two grid-calibration tests are described in the next two subsections. The descriptions include demonstrations that the Tensar SS20 biaxial geogrid used in the pavement-design example matches the laboratory-test responses. The grid tensile stiffness is measured by the Multiple Aperture Tensile test that is described in the next subsection. The material-genesis procedure to embed a geogrid within the granular material is described in the final subsection.

## **2.1 Grid-Modeling Methodology: Grid Set**

The grid-modeling methodology that uses parallel-bonded contacts draws upon the work of Stahl and co-workers (Jas et al. [2015a, 2015b]; Stahl and te Kamp [2013, 2012]; Stahl et al. [2014]; Stahl and Konietzky [2011]; Stahl [2011]; Konietzky et al. [2004]), with the primary contribution being the closed-form expressions defining the sizes and locations of the balls and the radii of the parallel bonds as summarized by Stille (2015).<sup>3</sup> The grid-modeling methodology that uses beamed contacts was developed for MnDOT and is described in this document. McDowell and co-workers (McDowell et al. [2006]; Chen et al. [2013]) describe a similar grid-modeling methodology in which the geogrid consists of spherical balls joined by parallel bonds. Qian and co-workers (Qian et al. [2015]) describe the modeling of granular material as discrete polyhedral grains in which rigid geogrids may be embedded, with the mechanical behavior of the discrete system being simulated by the three-dimensional discrete-element program BLOKS3D.

The grid-modeling methodology is summarized as follows. The grid consists of strings of overlapping spherical balls joined by either parallel bonds or beamed contacts. The parallel bonds or beamed contacts provide the structural properties of the grid, and the spherical balls provide the surface for grid-object interaction, which occurs at the grid-grain and grid-grid contacts. Each biaxial grid junction consists of two intersecting ribs, and for the parallel-bonded system, additional material in the form of join balls that increases the junction stiffness. Each triaxial grid junction consists of three intersecting ribs.

---

<sup>3</sup> Tensar International Limited is acknowledged for its research efforts modeling geogrids and granular soils, and in particular, for granting access to the grid-modeling methodology developed on its behalf by Itasca Consultants GmbH. Tensar is commended for its willingness to grant this access, fostering development of these models to benefit the wider industry.

There are five types of contacts in the modeled system: grain-grain, grid-grid, grid-grain, grid-wall and grain-wall. The grain-grain contacts employ the hill contact model, the grid-grid contacts employ either the linear parallel bond contact model or the beam contact model, and the remaining three contact types employ the linear contact model. The hill contact model provides the behavior of an infinitesimal, nonlinear elastic (no tension) and frictional interface that carries a compressive surface-interaction force and may carry a tensile moisture force. The parallel-bond and beam contact models provide the behavior of a finite-size, linear elastic and bonded interface that carries a force and moment. The interface of the parallel-bonded contact model has a circular cross section, while the interface of the beam contact model has a rectangular cross section. The linear contact model provides the behavior of an infinitesimal, linear elastic (no tension) and frictional interface that carries a force. The hill contact model is described in Potyondy (2019c), the parallel-bond and linear contact models are described in Itasca (2019), and the beam contact model is described in Potyondy (2019a).

Each grid rib behaves either as an elastic beam of circular cross section with varying radius along its length (parallel-bonded contacts), or as a prismatic and bisymmetrical elastic beam with varying width and height along its length (beamed contacts). The grid behaves as an elastic body; it will not break, and it will return to its original shape when unloaded. The grid methodology of Stahl and te Kamp (2013) employed a parallel-bond radius and stiffness decreasing law to allow the grid to exhibit nonlinear and plastic behavior. The stiffness decreasing law is excluded from the present methodology, which is believed to be sufficient for cases in which the grid experiences small-deformation loading for which rib tensile strains remain less than three percent and junction rotations remain less than two degrees.

The geogrids are specified as a grid set that consists of identical flat geogrids oriented perpendicular to the global  $z$ -axis, and spaced evenly in the  $z$ -direction. When embedding the grid set within a granular material, the grid set is aligned with the specimen axis and positioned within either a polyaxial or cylindrical cell. The grid-set parameters are listed in Table 1, and the modeled system is shown in Figure 4. Grid deformation causes strain energy to be stored in the contacts that join the grid balls to one another — expressions for the strain energy in the parallel-bonded and beamed contacts are given in Itasca (2019)<sup>4</sup> and Potyondy (2019a), respectively. The strain energy stored in the grid set ( $E_g$ ,  $E_g \geq 0$ ) is given by the FISH variable **gd\_Estr** and provides a scalar index of the load being carried by the grid.

---

<sup>4</sup> In documentation set at PFC: PFC Model Objects: Contacts and Contact Models: Contact Models: Built-in Contact Models: Linear Parallel Bond Model: Energy Partitions.

**Table 1 Grid Set Parameters**

Parameter	Type	Range	Default	Description
<b>Grid set group:</b>				
$n_g$ , <b>gd_ng</b>	INT	$[1, \infty)$	1	number of grids
$s_z$ , <b>gd_sz</b>	FLT	$(0.0, \infty)$	NA	grid spacing (in z-direc.)
$\{n_x, n_y\}$ , <b>gd_n{x,y}</b>	INT	$[1, \infty)$	$\{1, 1\}$	number of cross elements in x and y direcs.
$\mathbf{c}$ , <b>gd_c</b>	VEC	$[\mathbb{R}, \mathbb{R}, \mathbb{R}]$	<b>0</b>	position of node ball of bottom back left cross element (see Figure 4)
$C_t$ , <b>gd_tips</b>	INT	$\{0, 1\}$	0	grid-tip code $\begin{cases} 0, & \text{remove grid tips} \\ 1, & \text{keep grid tips} \end{cases}$
$C_g$ , <b>gd_beamed</b>	INT	$\{0, 1, 2\}$	0	grid-type code $\begin{cases} 0, & \text{biaxial with parallel-bonded contacts} \\ 1, & \text{biaxial with beamed contacts} \\ 2, & \text{triaxial with beamed contacts} \end{cases}$
$D_n$ , <b>gd_Dn</b>	FLT	$(0.0, \infty)$	NA	diameter of node ball
$l_r$ , <b>gd_lr</b>	FLT	$(0.0, \infty)$	NA	length of rib
$\kappa_r$ , <b>gd_Drat</b>	FLT	$(0.0, 1.0)$	0.9	diameter ratio of first rib ball $(\kappa_r = D_c^{(1)}/D_n, C_g = 0)$
$n_c$ , <b>gd_nc</b>	INT	$[1, \infty)$	7	core balls per half rib ( $C_g = 0$ )
$D_m$ , <b>gd_Dm</b>	FLT	$(0.0, \infty)$	NA	diameter of mid-rib ball ( $C_g \neq 0$ )
$\bar{R}_n$ , <b>gd_pbRadNd</b>	FLT	$(0.0, \infty)$	NA	parallel-bond radius at node ball $(C_g = 0)$
$\bar{R}_m$ , <b>gd_pbRadMid</b>	FLT	$(0.0, \infty)$	NA	parallel-bond radius at mid rib $(\bar{R}_m \leq \bar{R}_n, C_g = 0)$
$\bar{\lambda}_j$ , <b>gd_pbRmulJn</b>	FLT	$(0.0, \infty)$	1.0	parallel-bond radius multiplier of join balls ( $C_g = 0$ )
$b_n$ , <b>gd_xCbNd</b>	FLT	$(0.0, \infty)$	NA	rib cross-sectional width (aligned with xy-plane) at node ball ( $C_g \neq 0$ )
$h_n$ , <b>gd_xChNd</b>	FLT	$(0.0, \infty)$	NA	rib cross-sectional height (aligned with z-axis) at node ball ( $C_g \neq 0$ )
$b_m$ , <b>gd_xCbMid</b>	FLT	$(0.0, \infty)$	NA	rib cross-sectional width (aligned with xy-plane) at mid rib ( $b_m \leq b_n, C_g \neq 0$ )



$h_m, \mathbf{gd\_XChMid}$	FLT	$(0.0, \infty)$	NA	rib cross-sectional height (aligned with z-axis) at mid rib ( $h_m \leq h_n, C_g \neq 0$ )
$C_e, \mathbf{gd\_latExtent}$	INT	$\{0,1\}$	0	exclusion region lateral-extent existence code $\begin{cases} 0, & \text{exists} \\ 1, & \text{does not exist} \end{cases}$
<b>Material properties group:</b>				
$\alpha_g, \mathbf{gd\_dampFac}$	FLT	$[0.0, 0.7]$	0.0	local-damping factor
$\rho_g, \mathbf{gd\_density}$	FLT	$(0.0, \infty)$	NA	density (set grid-ball density: $\rho_b = \rho_g$ , does not account for grid-ball overlap)
$E_g^*, \mathbf{gd\_emod}$	FLT	$[0.0, \infty)$	0.0	effective modulus ( $C_g = 0$ )
$\kappa_g^*, \mathbf{gd\_krat}$	FLT	$[0.0, \infty)$	0.0	stiffness ratio ( $C_g = 0$ )
$E_g, \mathbf{gd\_E}$	FLT	$[0.0, \infty)$	0.0	Young's modulus ( $C_g \neq 0$ )
$\nu_g, \mathbf{gd\_nu}$	FLT	$(-1.0, 0.5]$	0.0	Poisson's ratio ( $C_g \neq 0$ )
$E_{gs}^*, \mathbf{gd\_gsemod}$	FLT	$[0.0, \infty)$	0.0	grid-surface effective modulus
$\kappa_{gs}^*, \mathbf{gd\_gskrat}$	FLT	$[0.0, \infty)$	0.0	grid-surface stiffness ratio
$\mu_{gs}, \mathbf{gd\_gsfric}$	FLT	$[0.0, \infty)$	0.0	grid-surface friction coefficient



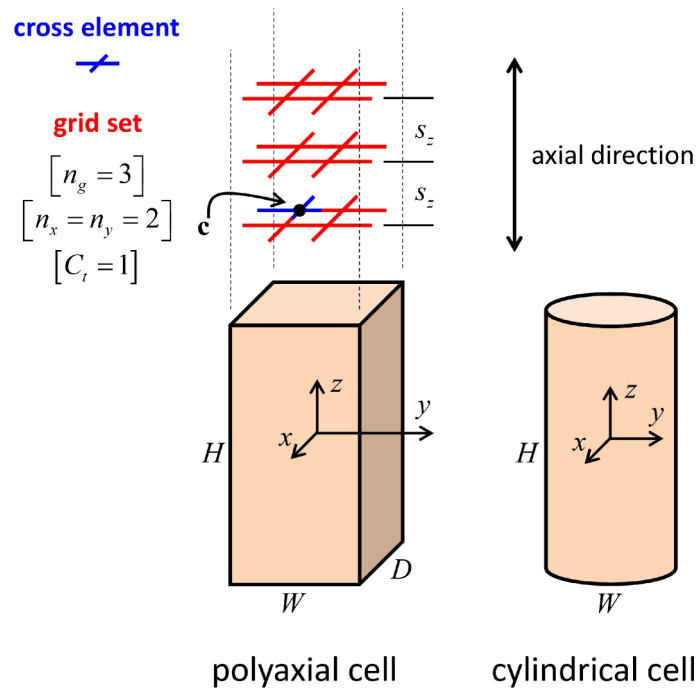


**Figure 4** Material vessels and grid set consisting of three biaxial grids, each of which has four cross elements shown in Figures 5 and 10.

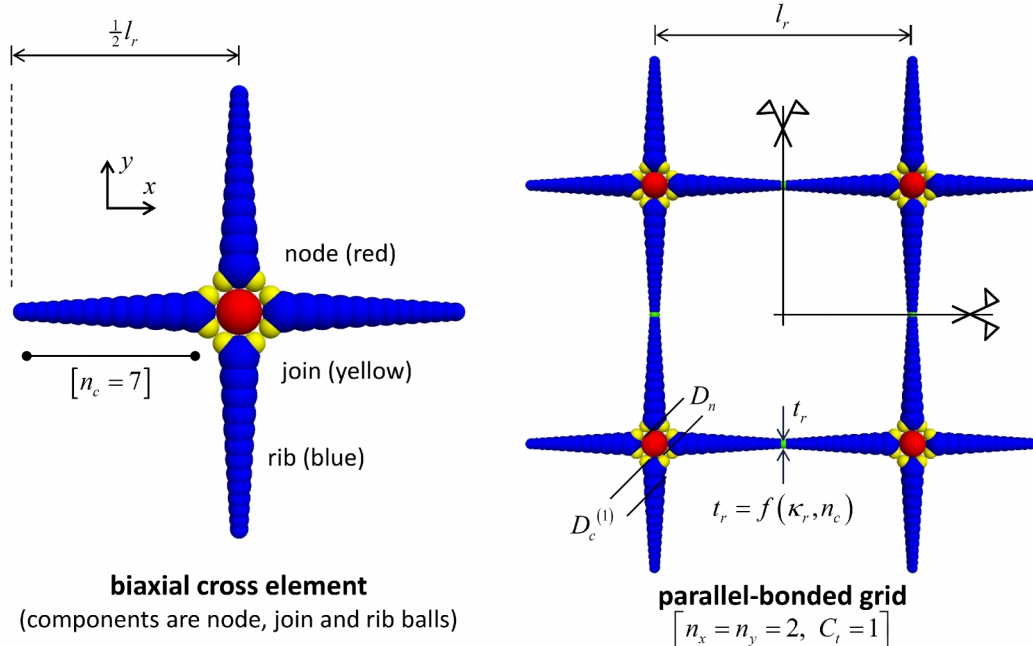


**Figure 5** Cross element and biaxial parallel-bonded grid consisting of four cross elements.

The grid set consists of  $n_g$  identical grids. Each grid is flat and lies in the  $xy$ -plane, and the grids are spaced evenly along the  $z$ -axis at a distance of  $s_z$ . A grid consists of identical cross elements, with  $n_x$  and  $n_y$  cross elements in the  $x$ - and  $y$ -directions, respectively. A biaxial cross element consists of one node ball with a half rib in both directions (see Figures 5 and 10), while a triaxial cross element consists of one node ball with a half rib in three directions (see Figure 11)<sup>5</sup>. The bottom back left cross element of the grid set is centered at  $\mathbf{c}$ . The presence of cross-element tips at the outside edge of the grid set is controlled by the grid-tip code  $C_t$ .

The grids that consist of either parallel-bonded contacts or beamed contacts are described in their own sections that follow.

### 2.1.1 Parallel-bonded grid

The geometry of a cross element is defined by the node-ball diameter ( $D_n$ ), the diameter ratio of the first rib ball ( $\kappa_r = D_c^{(1)} / D_n$ ), the rib length ( $l_r$ ), and the number of core balls per half rib ( $n_c$ ). The minimum rib thickness ( $t_r$ ) is a function of  $\kappa_r$  and  $n_c$ . The parallel-bond radii in the grid are defined by the parallel-bond radii at the node and mid rib ( $\bar{R}_n$  and  $\bar{R}_m$  along with an exponential variation along each half rib) and the parallel-bond radius multiplier of the join balls ( $\bar{\lambda}_j$ ). The material properties of the grid are defined by the local-damping factor, density, effective modulus and stiffness ratio ( $\alpha_g$ ,  $\rho_g$ ,  $E_g^*$  and  $\kappa_g^*$ ). The material properties of the grid surface are defined by the grid-surface effective modulus, stiffness ratio and friction coefficient ( $E_{gs}^*$ ,  $\kappa_{gs}^*$  and  $\mu_{gs}$ ).<sup>6</sup>

<sup>5</sup> Each cross element is symmetric; thus, there is no differentiation between the transverse (TD) and longitudinal (LD) directions. Such a differentiation was employed by Stahl and te Kamp (2013). The pavement-design package can be modified to account for this by making the TD and LD directions correspond with the  $x$ - and  $y$ -directions, and replacing  $l_r$  and  $n_c$  with  $\{l_{\pi}, l_{\nu}\}$  and  $\{n_{\pi}, n_{\nu}\}$ , respectively.

<sup>6</sup> The linear contact model is installed at the grid-grain and grid-grid contacts that may form after grid creation; the stiffness and friction coefficient of these contacts are set based on the specified deformability and friction coefficient. The linear contact model is also installed at the grid-wall contacts that may form after grid creation; the walls are frictionless, and the normal stiffness of these contacts is set based on the effective modulus of the material vessel. [The linear contact bond model is installed at grid-grain and grid-grid contacts to facilitate visual inspection of these contacts via the contact plot item (using Color By: Text Val: model name). The linear contact bond model is unbonded, and thus, its behavior is identical to that of the linear contact model.]

The parallel bonds in the grid are assigned infinite strengths to preclude bond breakage, the parallel-bond stiffnesses are set based on  $E_g^*$  and  $\kappa_g^*$ , the parallel-bond radii at each join ball are set based on  $\bar{\lambda}_j$  and join-ball diameter, and the parallel-bond radii along each half rib are set via Eq. (6).<sup>7</sup>

The closed-form expressions defining the sizes and locations of the balls and the radii of the parallel bonds are provided in the remainder of this subsection. The balls of a cross element half rib are shown in Figure 6. The half rib consists of one node ball, two join balls, and a string of rib balls, with the rib balls being divided into core-rib balls, mid-rib balls and a tip-rib ball. The sizes of the core-rib balls satisfy the relation:

$$\frac{1}{2}l_r = \frac{1}{2}D_n + \sum_{b=1}^{n_c} \alpha^{(b-1)} \kappa_r D_n. \quad (1)$$

This relation is rewritten in the form:

$$f(\alpha) = \frac{D_n - l_r}{2\kappa_r D_n} + \sum_{b=1}^{n_c} \alpha^{(b-1)} = 0. \quad (2)$$

The constant,  $\alpha$ , is found by solving the above expression via Newton-Raphson iteration. The diameters and positions of the rib balls are expressed in terms of alpha as follows. The diameters and positions of the core-rib balls:

$$\begin{aligned} D_c^{(b)} &= \alpha^{(b-1)} \kappa_r D_n, \quad b \in \{1, 2, \dots, n_c\} \\ s_c^{(b)} &= s_c^{(b-1)} + \frac{1}{2} D_c^{(b-1)} + \frac{1}{2} D_c^{(b)}, \quad D_c^{(0)} = D_n, \quad s_c^{(0)} = 0, \quad b \in \{1, 2, \dots, n_c\}. \end{aligned} \quad (3)$$

The diameters and positions of the mid-rib balls:

$$\begin{aligned} D_m^{(b)} &= \frac{2\alpha}{(1+\alpha)^2} (D_c^{(b)} + D_c^{(b+1)}), \quad D_m^{(n_c)} = 2D_c^{(n_c)} - D_m^{(n_c-1)}, \quad b \in \{1, 2, \dots, n_c-1\} \\ s_m^{(b)} &= s_c^{(b)} + \frac{1}{2} D_c^{(b)}, \quad b \in \{1, 2, \dots, n_c\}. \end{aligned} \quad (4)$$

<sup>7</sup> The stiffnesses of the linear component of the linear parallel bond contact model are set to zero such that all load is carried in the bond — i.e., the linear force arising from ball-ball overlap always remains equal to zero.

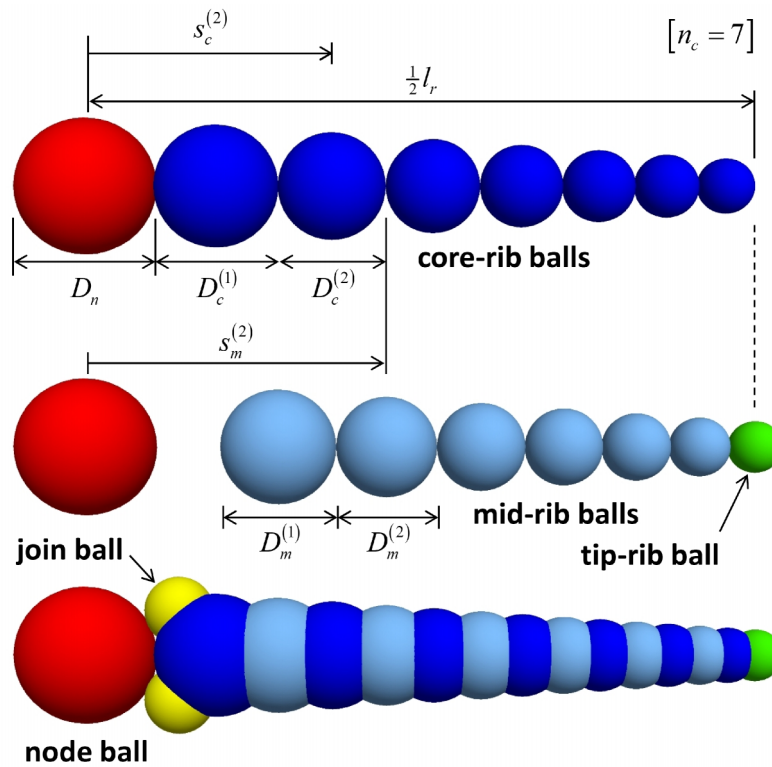


**Figure 6** Cross element half rib showing node ball, join balls and rib balls.

There is also a tip-rib ball that lies between adjoining cross elements, and its diameter and position are obtained by treating it as a mid-rib ball. The diameters and positions of the join balls (with reference to Figure 7):

$$D_j = \frac{1}{2} D_n$$

$$\beta = \frac{\pi}{4} - \varphi, \quad \varphi = \sin^{-1} \left( \frac{D_j}{D_n + D_j} \right). \quad (5)$$

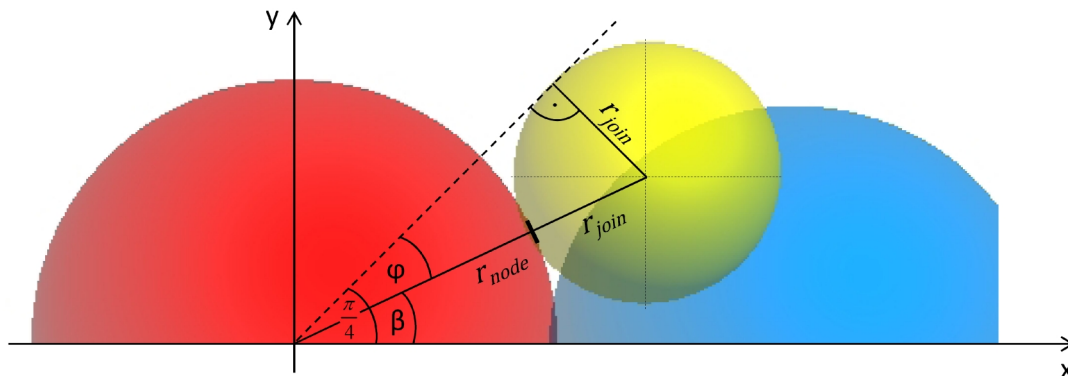


**Figure 7** Cross element half rib showing location of the top join ball.

The parallel-bond radii in the geogrid vary exponentially along each half rib (see Figure 8):

$$\begin{aligned}\bar{R} &= ae^{bs}, \quad \frac{1}{2}D_n \leq s \leq \frac{1}{2}l_r \\ \text{with } a &= \bar{R}_n \exp\left(\frac{-bD_n}{2}\right) \\ b &= \ln\left(\frac{\bar{R}_n}{\bar{R}_m}\right) \frac{2}{D_n - l_r}\end{aligned}\quad (6)$$

where  $s$  is measured from the node-ball center. Each join ball has four parallel bonds joining it to the node ball, the adjacent join ball, and the first two rib balls (see Figure 9).

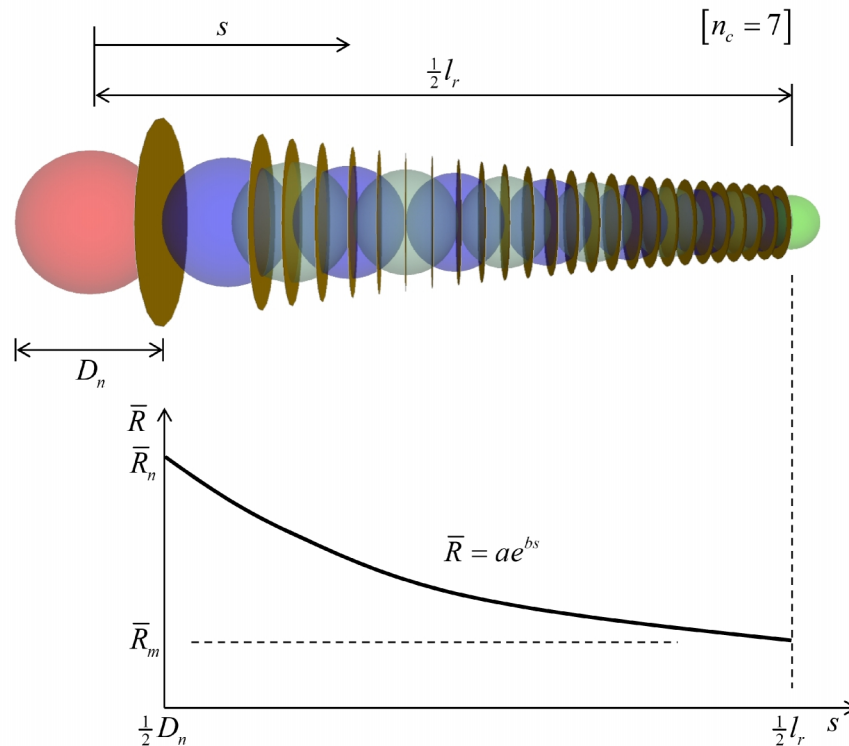


**Figure 8** Cross-element half rib showing variation of parallel-bond radius from node ball to mid rib. Each parallel-bonded interface is drawn as a disk with radius equal to parallel-bond radius.

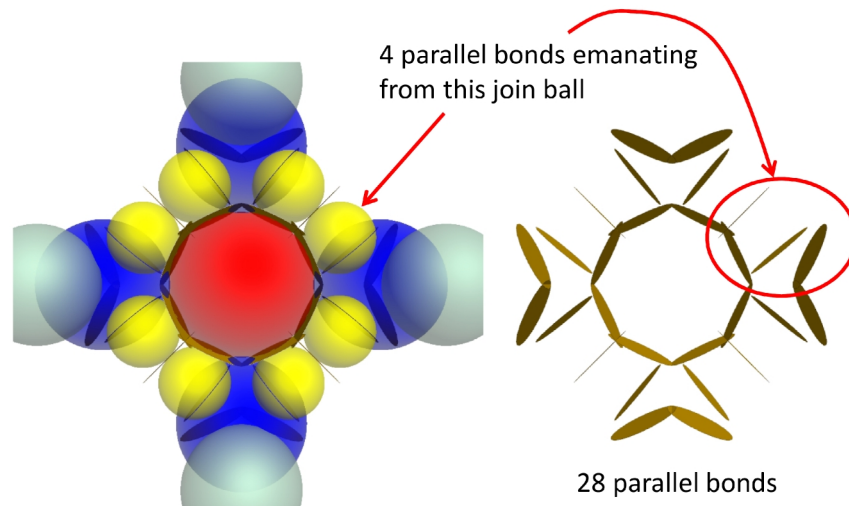


**Figure 9** *Parallel bonds emanating from the join balls at a cross-element node.*

### 2.1.2 Beamed grid

The geometry of both biaxial and triaxial beamed grid cross elements is defined by the node-ball diameter ( $D_n$ ), the rib length ( $l_r$ ) and the mid-rib ball diameter ( $D_m$ ) as shown in Figures 10 and 11. A string of balls with diameter  $D_m$  are created between the node and mid-rib balls, with the overlap being distributed equally among all contacts in the string. The width and height of the rib cross section are defined by the width and height at the node ( $b_n$  and  $h_n$ ) and mid rib ( $b_m$  and  $h_m$ ), along with an exponential variation along each half rib. The exponential variations are given by Eq. (6), with the width and height replacing the parallel-bond radius in this expression. The material properties of the beamed grid are defined by the local-damping factor and density ( $\alpha_g, \rho_g$ ) as well as the Young's modulus and Poisson's ratio of the grid material ( $E_g$  and  $\nu_g$ ). The material properties of the grid surface are defined by the grid-surface effective modulus, stiffness ratio and friction coefficient ( $E_{gs}^*, \kappa_{gs}^*$  and  $\mu_{gs}$ ).<sup>8</sup>

<sup>8</sup> The linear contact model is installed at the grid-grain and grid-grid contacts that may form after grid creation; the stiffness and friction coefficient of these contacts are set based on the specified deformability and friction coefficient. The linear contact model is also installed at the grid-wall contacts that may form after grid creation; the walls are frictionless, and the normal stiffness of these contacts is set based on the effective modulus of the material vessel. [The linear contact bond model is installed at grid-grain and grid-grid contacts to facilitate visual inspection of these contacts via the contact plot item (using Color By: Text Val: model name). The linear contact bond model is unbonded, and thus, its behavior is identical to that of the linear model.]

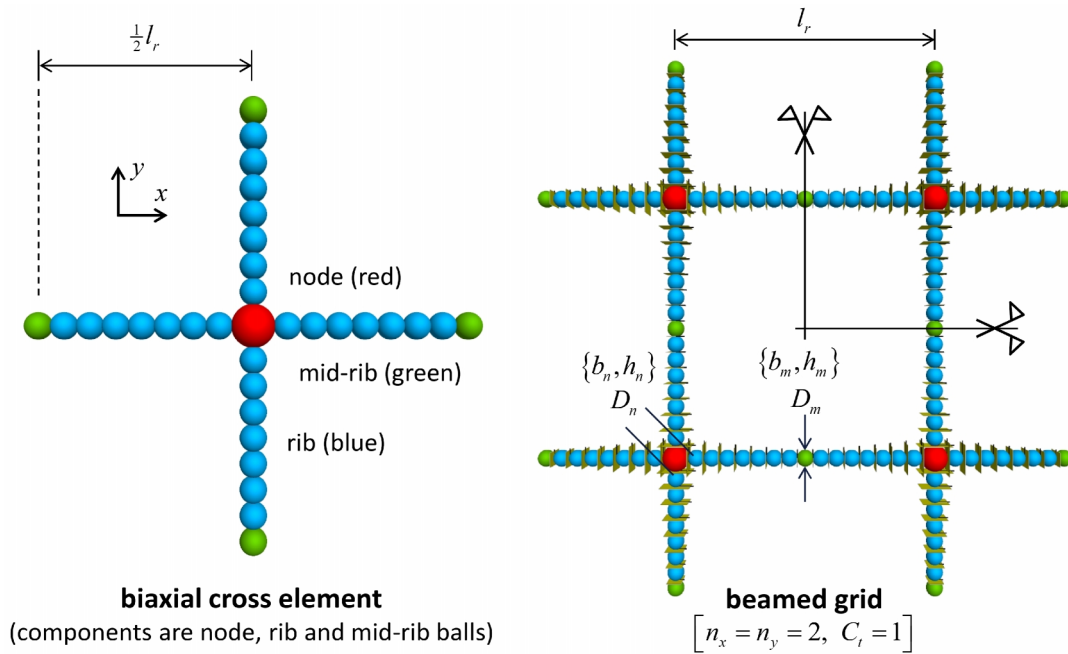


**Figure 10** Cross element and biaxial beamed grid consisting of four cross elements.

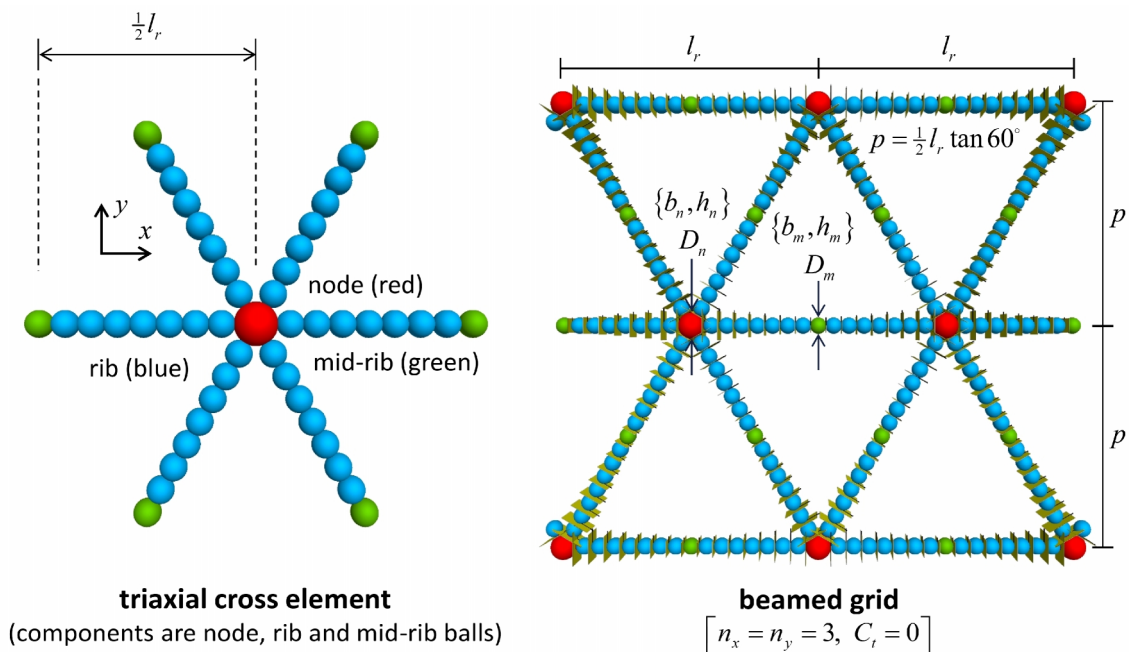


**Figure 11** Cross element and triaxial beamed grid with tips removed.



## 2.2 Grid Calibration: Single Rib Tensile Tests

The rib tensile stiffnesses of a biaxial geogrid are measured by performing Single Rib Tensile (SRT) tests in the transverse (TD) and longitudinal (LD) directions. The two ribs emanating from a grid junction and aligned in the desired direction are clamped at the junctions at their ends (as shown in Figure 12). One end is fixed, and a constant velocity is applied to the other end while monitoring the applied displacement and associated force. The displacement is expressed as a strain using the length between clamps as the gauge length. The force-extension curves for a Tensar SS20 biaxial geogrid are shown in Figure 13, in which the black line is the average curve from five laboratory tests. The force-extension behaviors are similar in the TD and LD directions. The force-extension curve is linear for extension of less than three percent, at which point the slope begins to decrease. The slope of the force-extension curve is a measure of stiffness. The stiffness decrease indicates material softening, perhaps as the result of plastic yielding of the material at the rib center. A permanent rib extension would be associated with plastic yielding — it is not known to the author if a permanent rib extension has occurred.

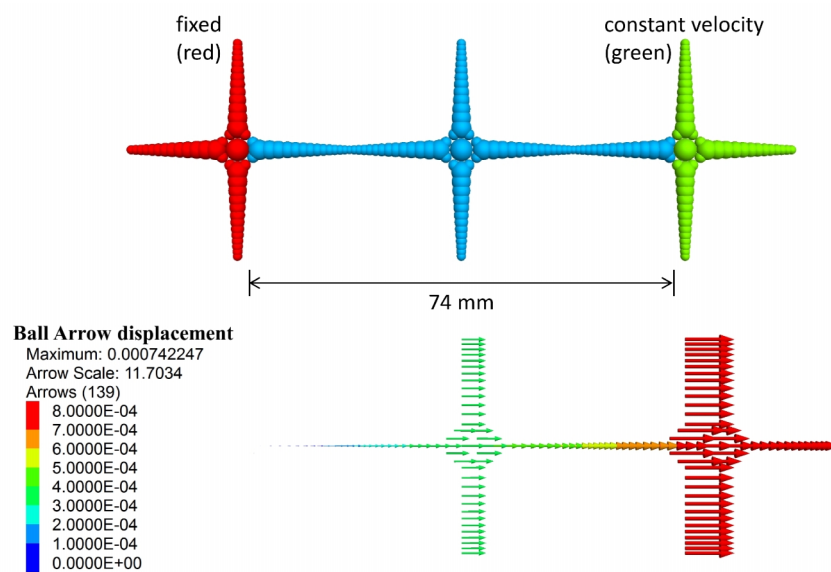


**Figure 12** The undeformed SS20 parallel-bonded grid at the start of the SRT test (above), and the grid displacement field at the end of the SRT test (below).



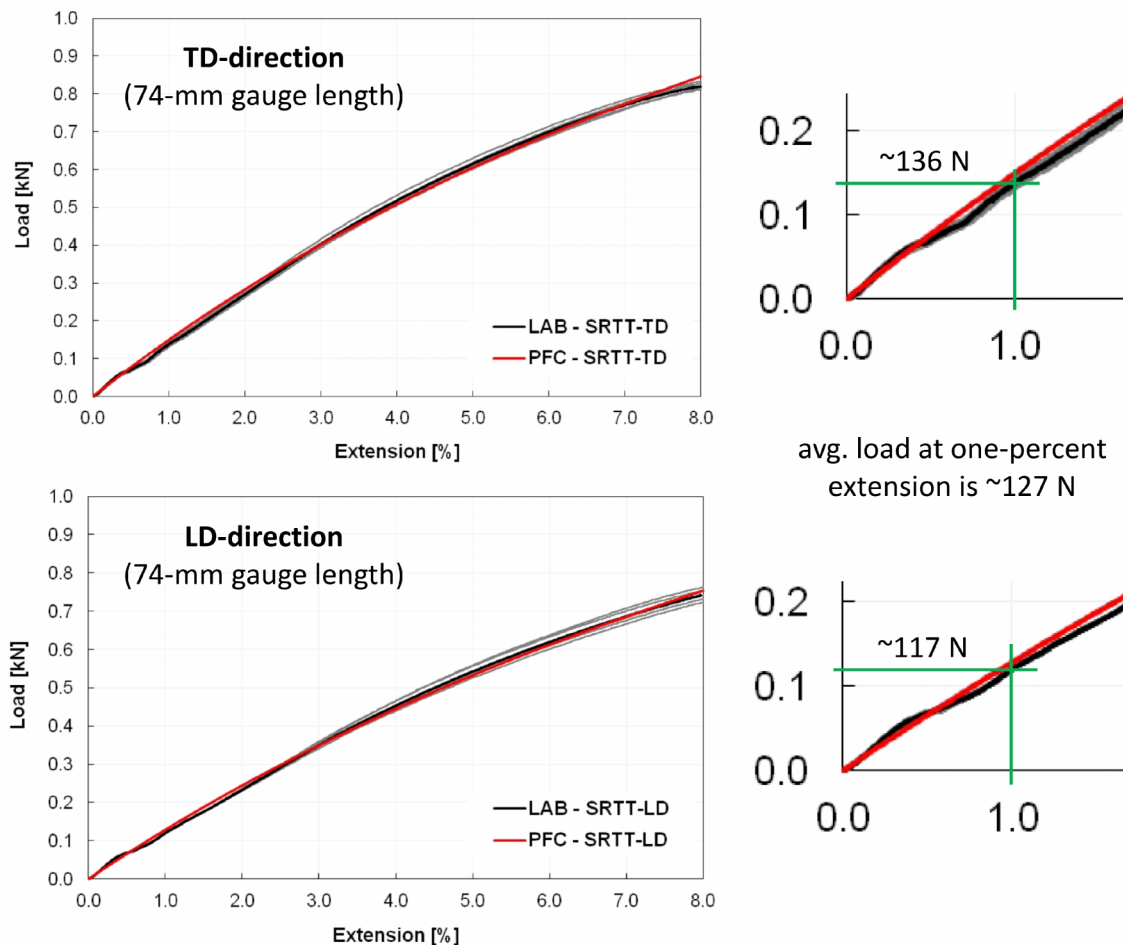


**Figure 13** Force versus extension for a Tensar SS20 biaxial geogrid loaded in the TD and LD directions during SRT tests. (From Figs. 8 and 9 of Stahl and te Kamp [2013] in which force is denoted as load.)

The rib tensile stiffnesses of a triaxial geogrid are measured by performing Single Rib Tensile (SRT) tests in the three rib directions (30, 90 and 150 degrees). The two ribs emanating from a grid junction and aligned in the desired direction are clamped at the junctions at their ends (as shown in Figure 14). One end is fixed, and a constant velocity is applied to the other end while monitoring the applied displacement and associated force. The displacement is expressed as a strain using the length between clamps as the gauge length. The force-extension curves for a Tensar TX160 triaxial geogrid are shown in Figures 15 and 16, in which the black line is the average curve from five laboratory tests. The force-extension behaviors differ in the three directions, with the 90 degree rib direction that is aligned with the transverse/cross machine direction (TD) being the stiffest. The force-extension curves are linear for extension of less than three percent, at which point the slopes begin to decrease.

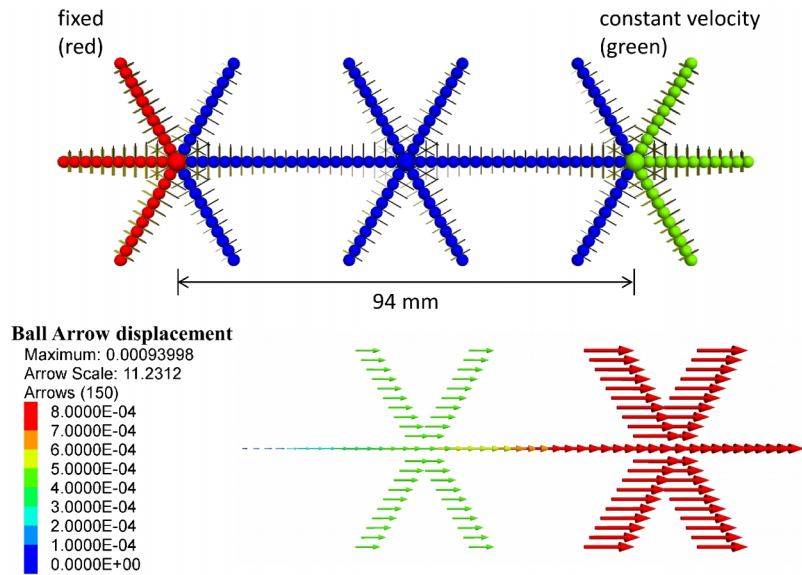


**Figure 14** The undeformed TX160 beamed grid at the start of the SRT test (above), and the grid displacement field at the end of the SRT test (below).

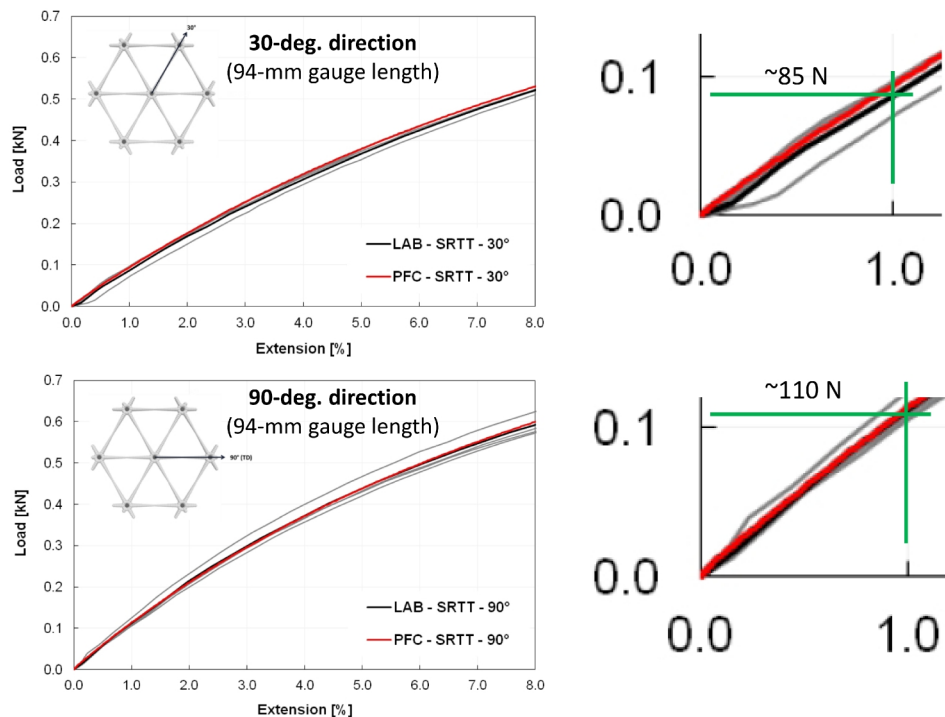


**Figure 15** Force versus extension for a Tensar TX160 triaxial geogrid loaded in the 30 and 90 degree directions during SRT tests. (From Figs. 11 and 12 of Stahl and te Kamp [2012] in which force is denoted as load.)

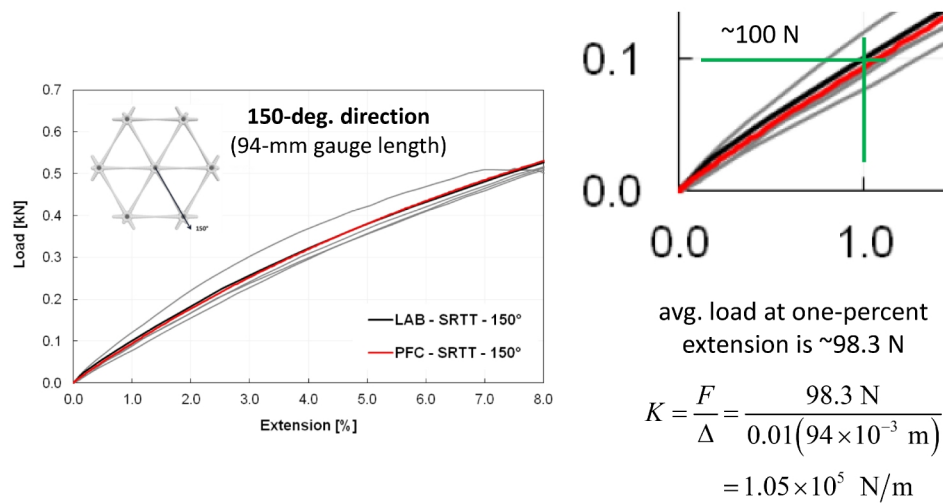


**Figure 16** Force versus extension for a Tensar TX160 triaxial geogrid loaded in the 150 degree direction during SRT tests. (From Fig. 13 of Stahl and te Kamp [2012] in which force is denoted as load.)

### 2.2.1 Parallel-bonded grid (biaxial)

The Tensar SS20 biaxial geogrid is modeled in the pavement-design example using the grid-set properties in Table 5. The synthetic geogrid is symmetric, with no differentiation between the TD and LD directions; therefore, the grid-set properties are chosen to match the average stiffness for extension less than three percent. The modeled system at the start and end of the SRT test is shown in Figure 12. The applied force is obtained by summing the out-of-balance forces of the balls that are assigned a constant velocity. The force-extension curve for quasi-static loading is shown in Figure 17. The modeled system matches the average force of 127 N at one-percent extension.

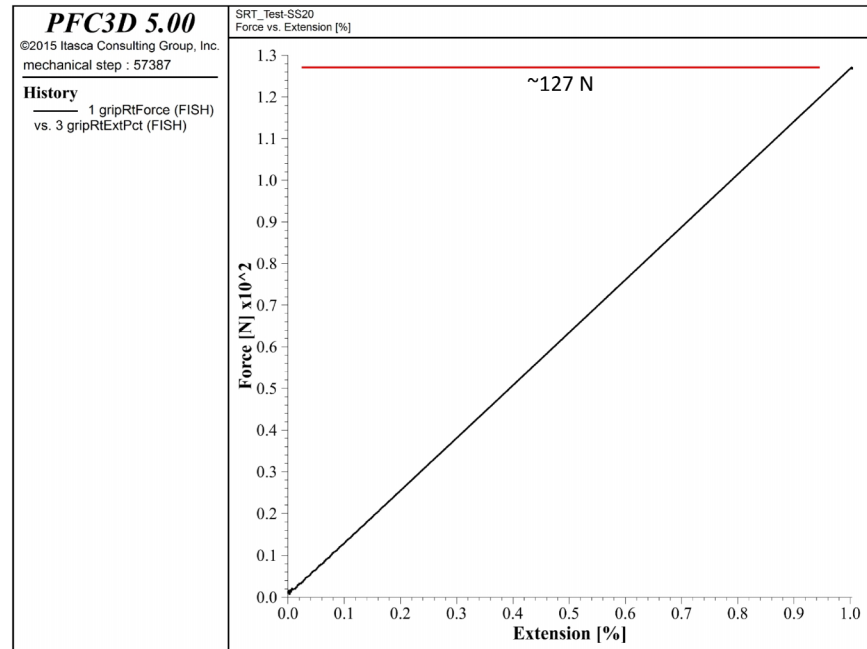


**Figure 17** Force versus extension for the SS20 parallel-bonded grid during the SRT test, and measurement of force for a one-percent extension.

### 2.2.2 Beamed grid (biaxial)

The Tensar SS20 biaxial geogrid is modeled using the grid-set properties in Table 2. The synthetic geogrid is symmetric, with no differentiation between the TD and LD directions; therefore, the grid-set properties are chosen to match the average stiffness for extension less than three percent. The modeled system at the start and end of the SRT test is shown in Figure 18. The modeled system matches the average force of 127 N at one-percent extension. Reducing the mid-rib ball diameter from 2.5 to 1.5 mm has a negligible effect on system stiffness.

**Table 2** Grid Set Properties of SS20 Beamed Grid\*

Property	Value
<b>Grid set group:</b>	
$n_g, s_z$ [mm], $\{n_x, n_y\}$ , $c$ [mm], $C_t$	1, NA, $\left\{ \begin{array}{l} \{3,1\}, \text{ SRT test} \\ \{7,7\}, \text{ ASM test} \end{array} \right\}$ , (0,0,0), 1
$C_g, D_n$ [mm], $l_r$ [mm], $D_m$ [mm]	1, 4.0, 39.0, 2.5
$b_n$ [mm], $b_m$ [mm], $h_n$ [mm], $h_m$ [mm], $C_e$	5.0, 2.0, 3.5, 3.5, 0
<b>Material properties group:</b>	
$\alpha_g, \rho_g$ [kg/m <sup>3</sup> ], $E_g$ [GPa], $\nu_g$	0.7, 950, 1.2, 0.42
$E_{gs}^*$ [MPa], $\kappa_{gs}^*$ , $\mu_{gs}$	500, 2.0, 0.5

\* Grid-set parameters are defined in Table 1.

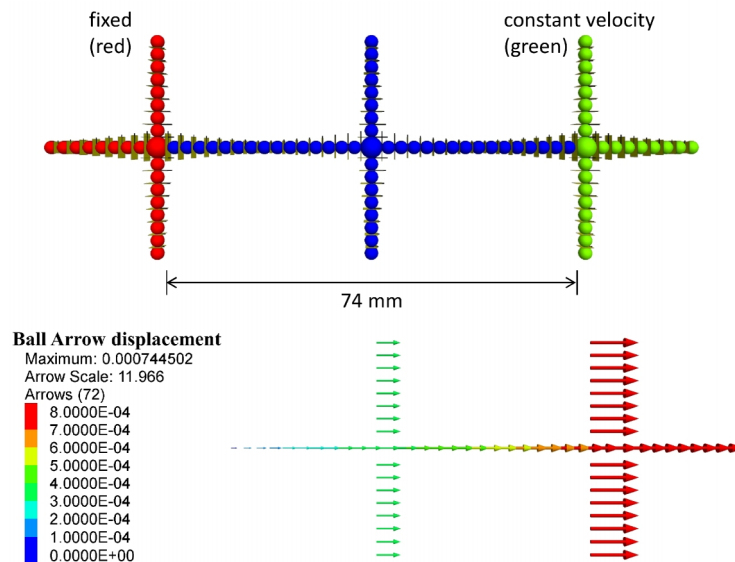


**Figure 18** The undeformed SS20 beamed grid at the start of the SRT test (above), and the grid displacement field at the end of the SRT test (below).

### 2.2.3 Beamed grid (triaxial)

The Tensar TX160 triaxial geogrid is modeled using the grid-set properties in Table 3. The synthetic geogrid is symmetric, with no differentiation between the three rib directions; therefore, the grid-set properties are chosen to match the average stiffness for extension less than three percent. The modeled system at the start and end of the SRT test is shown in Figure 14. The modeled system has a stiffness of  $1.05 \times 10^5$  N/m, which matches the average stiffness of the TX160 triaxial geogrid shown in Figure 16. Reducing the mid-rib ball diameter from 2.5 to 1.5 mm has a negligible effect on system stiffness.

**Table 3** Grid Set Properties of TX160 Beamed Grid\*

Property	Value
<b>Grid set group:</b>	
$n_g, s_z$ [mm], $\{n_x, n_y\}$ , $c$ [mm], $C_t$	1, NA, $\left\{ \begin{array}{l} \{3,1\}, \text{ SRT test} \\ \{7,9\}, \text{ ASM test} \end{array} \right\}$ , (0,0,0), 1
$C_g, D_n$ [mm], $l_r$ [mm], $D_m$ [mm]	2, 4.0, 47.0, 2.5
$b_n$ [mm], $b_m$ [mm], $h_n$ [mm], $h_m$ [mm], $C_e$	8.0, 4.0, 1.4, 1.4, 0
<b>Material properties group:</b>	

$\alpha_g, \rho_g [\text{kg/m}^3], E_g [\text{GPa}], \nu_g$	0.7, 950, 1.2, 0.42
$E_{gs}^* [\text{MPa}], \kappa_{gs}^*, \mu_{gs}$	500, 2.0, 0.5

\* Grid-set parameters are defined in Table 1.

### 2.3 Grid Calibration: Aperture Stability Modulus Tests

The junction torsional stiffness of a biaxial geogrid is measured by performing an Aperture Stability Modulus (ASM) test. A grid consisting of six by six apertures is clamped along its boundary as shown in Figure 19. The central junction is subjected to a twisting moment ( $M_t$ ) by applying a force ( $F$ ) to each of the four ribs emanating from the junction. The force is applied orthogonal to each rib at a fixed radial distance ( $r$ ) such that  $M_t = 4rF$ . The rotation of the central junction ( $\theta_t$ ) is measured. The torsional stiffness of the junction is given by

$$k_t = \frac{M_t}{\theta_t}. \quad (7)$$

The concept of torsional stiffness is embodied in the following structural system. The torsional stiffness of a twisted elastic shaft of length  $L$  loaded at its ends by equal and opposite twisting moments is given by Crandall et al. (1978, Eq. 6.10):

$$M_t = k_t \theta_t, \quad k_t = \frac{GJ}{L} \quad (8)$$

where  $G$  is the shear modulus, and  $J$  is the polar moment of inertia of the cross-sectional area about the axis of the shaft.

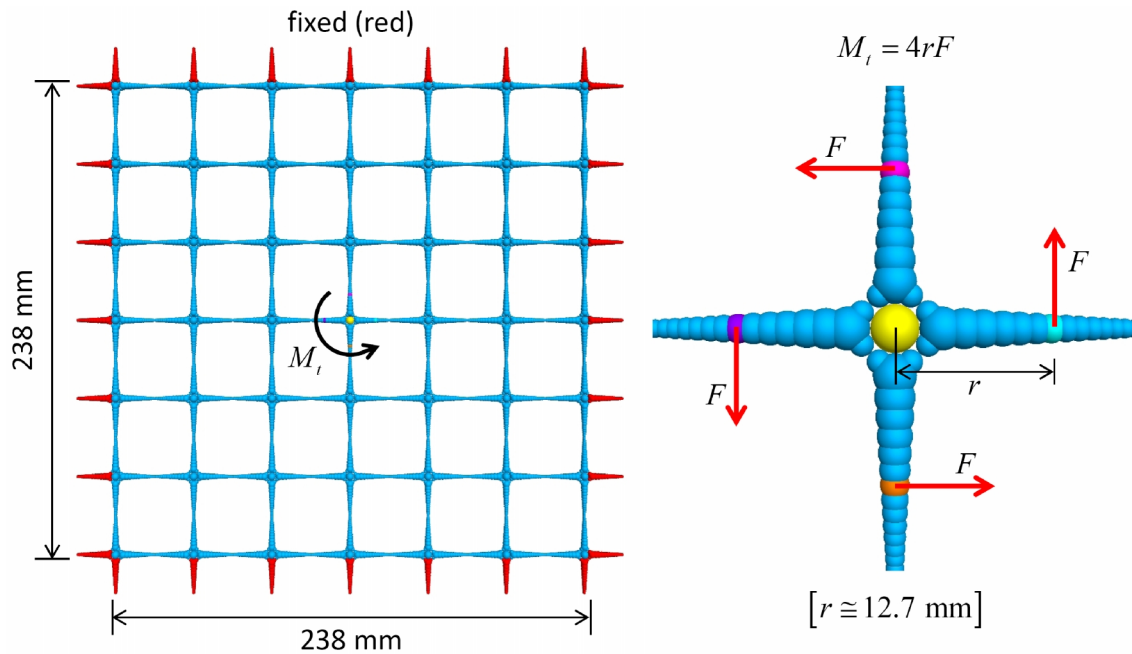


**Figure 19** The SS20 parallel-bonded grid showing the boundary conditions for the ASM test.

The moment-rotation curve for a Tensar SS20 biaxial geogrid is shown in Figure 20, in which the black line is the average curve from three laboratory tests. The moment-rotation curve is linear for rotation of less than two degrees, at which point the slope begins to increase. The slope of the moment-rotation curve is the torsional stiffness. The torsional stiffness increases with increasing rotation. This is a geometrically nonlinear effect denoted as stress stiffening.<sup>9</sup>

<sup>9</sup> The effect whereby the tensile membrane forces in a shell effectively increase the bending stiffness of the shell is called stress stiffening (Cook et al., 1989, p. 429). The tensile forces in the grid are similar to membrane forces in a shell. As the tensile forces in the grid are increased, the bending and torsional stiffnesses of the grid increase. The increase in torsional stiffness is described in the following analogous fashion. The geogrid provides a torsional elastic resistance to the deformation induced by the twisting moment, which aids in supporting the moment. The elastic resistance increases with increasing applied rotation.

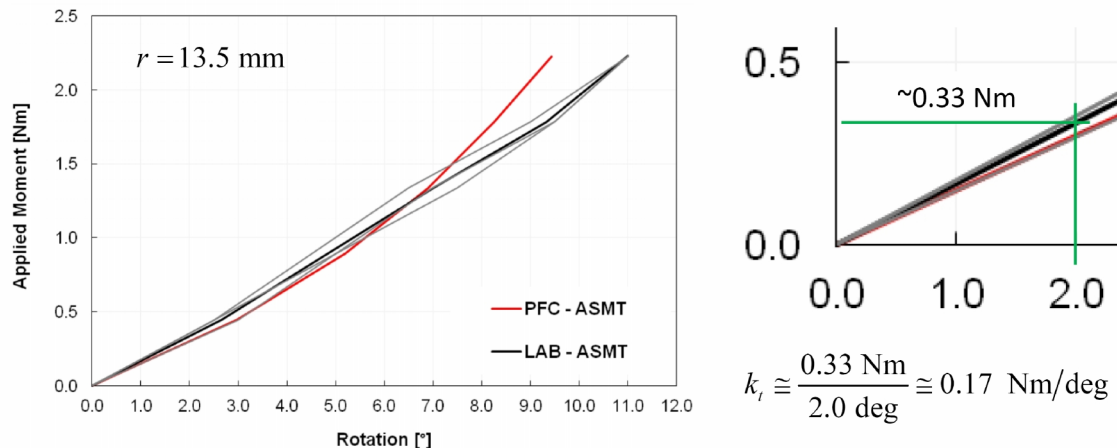


**Figure 20** Moment versus rotation for a Tensor SS20 biaxial geogrid during an ASM test. (From Fig. 12 of Stahl and te Kamp [2013].)

The junction torsional stiffness of a triaxial geogrid is measured by performing an Aperture Stability Modulus (ASM) test. A grid consisting of six pitches by five nodes is clamped along its boundary as shown in Figure 21. The central junction is subjected to a twisting moment ( $M_t$ ) by applying a force ( $F$ ) to each of the six ribs emanating from the junction. The force is applied orthogonal to each rib at a fixed radial distance ( $r$ ) such that  $M_t = 6rF$ . The rotation of the central junction ( $\theta_t$ ) is measured. The torsional stiffness of the junction is given by Eq. (7).

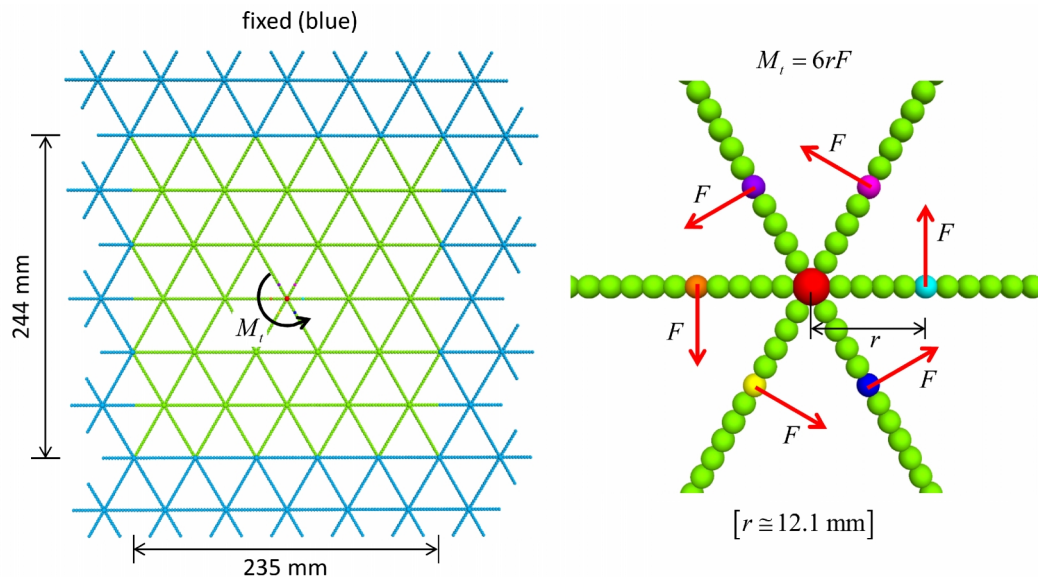


**Figure 21** The TX160 beamed grid showing the boundary conditions for the ASM test.



The moment-rotation curve for a Tensar TX160 triaxial geogrid is shown in Figure 22, in which the black line is the average curve from four laboratory tests. The moment-rotation curve is linear. The slope of the moment-rotation curve is the torsional stiffness. The average torsional stiffness of the four curves is 0.48 Nm/deg.

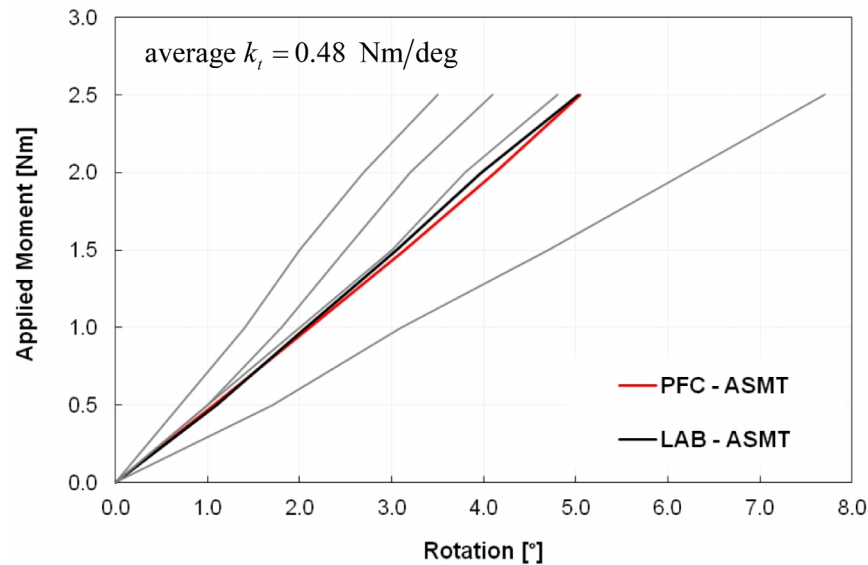


**Figure 22** *Moment versus rotation for a Tensar TX160 triaxial geogrid during an ASM test.* (From Fig. 23 of Stahl and te Kamp [2012].)

### 2.3.1 Parallel-bonded grid (biaxial)

The Tensar SS20 biaxial geogrid is modeled in the pavement-design example using the grid-set properties in Table 5. The modeled system is shown in Figure 19. A force of 5.9 N is applied to four grid balls, each of which is 12.7 mm from the central junction, such that the twisting moment is 0.30 Nm. Each force remains oriented in its initial global direction throughout the test. The model is run until the state of static equilibrium shown in Figure 23 has been obtained. The rotation is given by

$$\theta = \tan^{-1} \left( \frac{\Delta_y}{r} \right), \quad \text{valid for small-deformation} \quad (9)$$

where  $\Delta_y$  is the y-displacement of the loaded ball to the right of the central junction. The rotational stiffness is found to be 0.15 Nm/deg, which is 12 percent less than the experimental data. This match is deemed to be sufficient for the purposes of this study. It should be possible to obtain a better match, without sacrificing the match of the rib tensile stiffness, by adjusting the parallel-bond radius multiplier of the join balls ( $\bar{\lambda}_j$ ). Additional runs with applied forces of 20 and 40 N give

rotations of 5.9 and 9.5 deg, respectively, and rotational stiffnesses of 0.17 and 0.22 Nm/deg, respectively, which demonstrate that the model is exhibiting a stress-stiffening effect similar to that of the physical grid (see Figure 24).

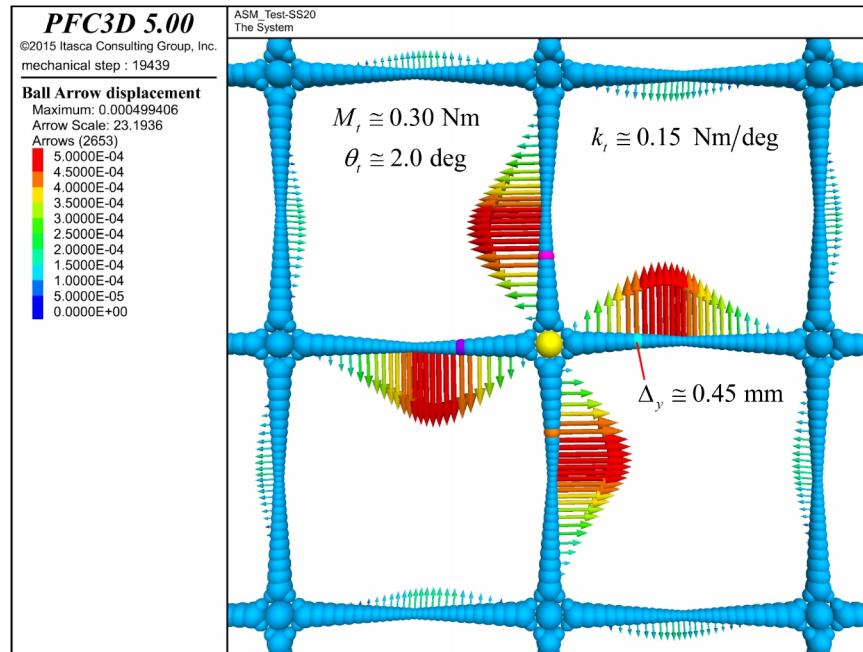


**Figure 23** Deformed grid and displacement field near the central junction of the SS20 parallel-bonded grid at the end of the ASM test with applied moment of 0.30 Nm.

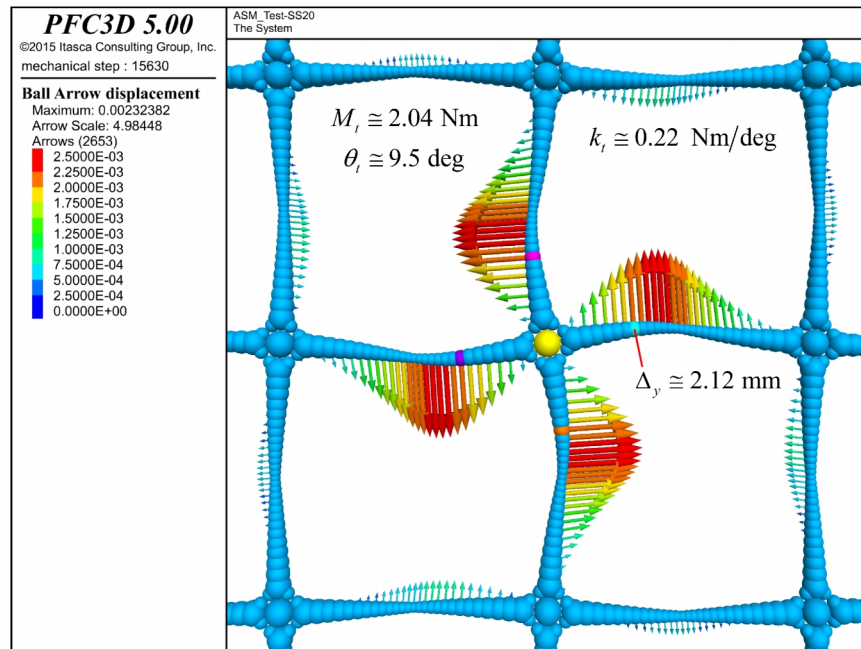


**Figure 24** Deformed grid and displacement field near the central junction of the SS20 parallel-bonded grid at the end of the ASM test with applied moment of 2.04 Nm.

### 2.3.2 Beamed grid (biaxial)

The Tensar SS20 biaxial geogrid is modeled using the grid-set properties in Table 2. The modeled system is similar to the system shown in Figure 19. A force of 5.9 N is applied to four grid balls, each of which is approximately 12.5 mm from the central junction, such that the twisting moment is 0.29 Nm. Each force remains oriented in its initial global direction throughout the test. The model is run until the state of static equilibrium shown in Figure 25 has been obtained. The rotation is given by Eq. (9). The rotational stiffness is found to be 0.17 Nm/deg, which matches the experimental data. Reducing the mid-rib ball diameter from 2.5 to 1.5 mm has a negligible effect on rotational stiffness.

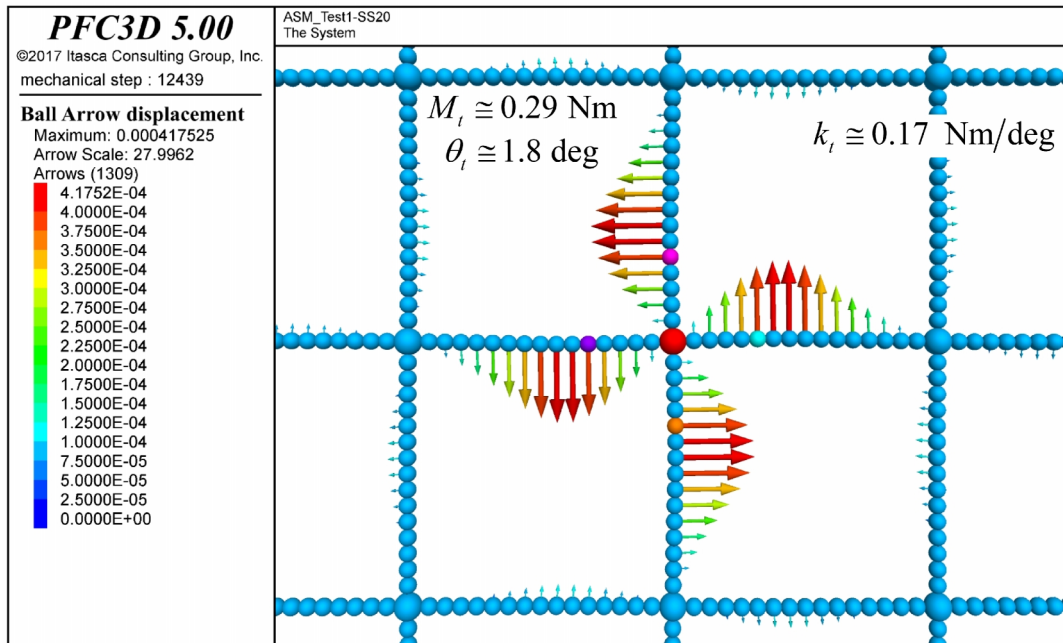


**Figure 25** Deformed grid and displacement field near the central junction of the SS20 beamed grid at the end of the ASM test.

### 2.3.3 Beamed grid (triaxial)

The Tensar TX160 triaxial geogrid is modeled using the grid-set properties in Table 3. The modeled system is shown in Figure 21. A force of 12.8 N is applied to six grid balls, each of which is approximately 12.1 mm from the central junction, such that the twisting moment is 0.93 Nm. Each force remains oriented in its initial global direction throughout the test. The model is run until the state of static equilibrium shown in Figure 26 has been obtained. The rotation is given by Eq. (9). The rotational stiffness is found to be 0.47 Nm/deg, which effectively matches the experimental data. Reducing the mid-rib ball diameter from 2.5 to 1.5 mm reduces the rotational stiffness by 8.5% to 0.43 Nm/deg.

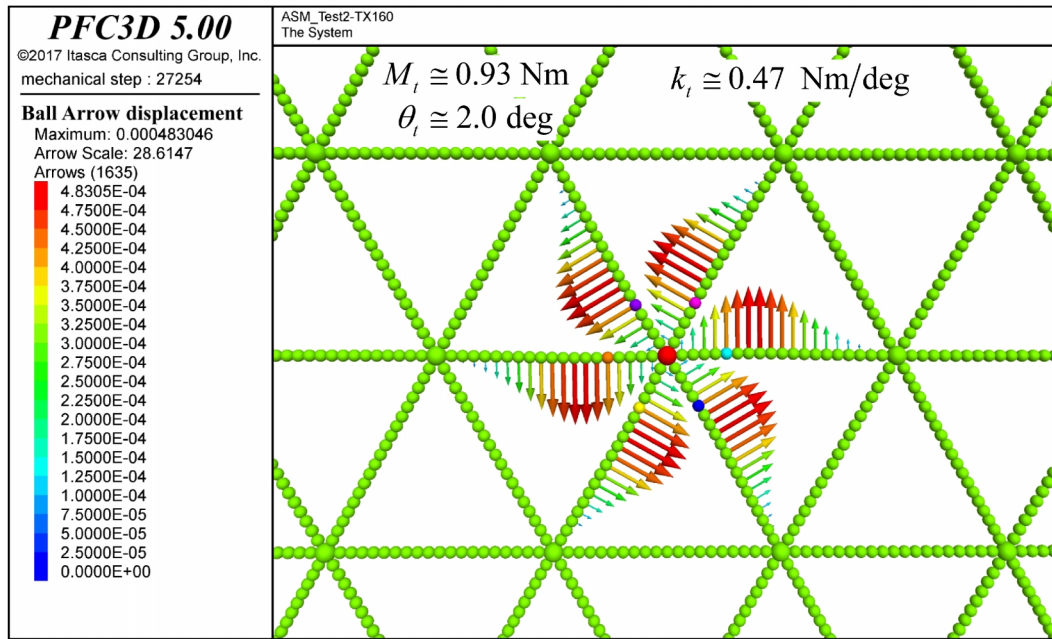


**Figure 26** Deformed grid and displacement field near the central junction of the TX160 beamed grid at the end of the ASM test.

## 2.4 Grid Calibration: Multiple Aperture Tensile Tests

The tensile stiffness of the geogrid is measured by performing a Multiple Aperture Tensile (MAT) test. A grid consisting of multiple apertures is clamped along its left and right edges as shown in Figure 27. The left edge is fixed, and a constant velocity is applied to the right edge while monitoring the applied displacement ( $\Delta$ ) and associated force ( $F$ ). The tensile stiffness is given by

$$k = \frac{F}{\Delta}. \quad (1.10)$$

The tensile stiffness is not constant, but varies as the number of apertures changes. An alternative stiffness measure that is independent of the number of apertures is the effective modulus given by

$$E' = \frac{kL}{A'} = \frac{kL}{D_n W} \quad (1.11)$$

where  $L$  is the horizontal distance between the clamps,  $A'$  is the effective area of the grid cross section,  $D_n$  is the diameter of the spherical node at each grid junction, and  $W$  is the effective width of the cross section —  $W$  extends beyond the clamped region by one-half aperture on each side.

### 2.4.1 Parallel-bonded grid (biaxial)

The Tensar SS20 biaxial geogrid is modeled in the pavement-design example using the grid-set properties in Table 5. A grid section consisting of four by four apertures is clamped along its right and left edges as shown in Figure 27. The grid is subjected to a one-percent extension, and the displacement field is shown in Figure 28. The grid effective modulus is 85.4 MPa .

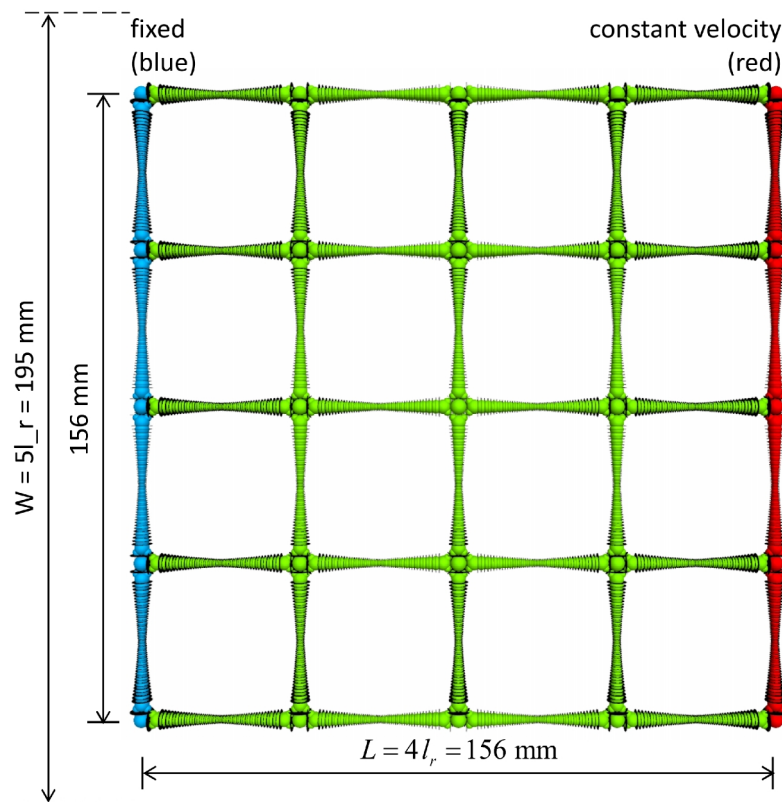


**Figure 27** The SS20 parallel-bonded grid showing the boundary conditions for the MAT test.

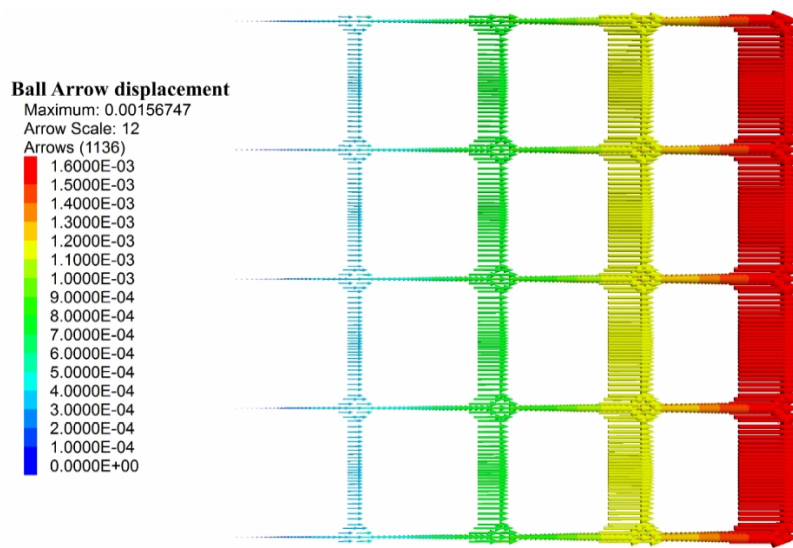


**Figure 28** *The displacement field of the S20 parallel-bonded grid at the end of the MAT test after application of one-percent extension.*

#### **2.4.2 Beamed grid (biaxial)**

The Tensar SS20 biaxial geogrid is modeled using the grid-set properties in Table 2. A grid section consisting of four by four apertures is clamped along its right and left edges as shown in Figure 29. The grid is subjected to a one-percent extension, and the displacement field is shown in Figure 30. The grid effective modulus is 85.8 MPa, which is approximately the same as for the parallel-bonded biaxial grid. This is the expected behavior, because both grids have the same rib tensile stiffness, and it is this stiffness that is being measured in a macroscopic sense by the MAT test.



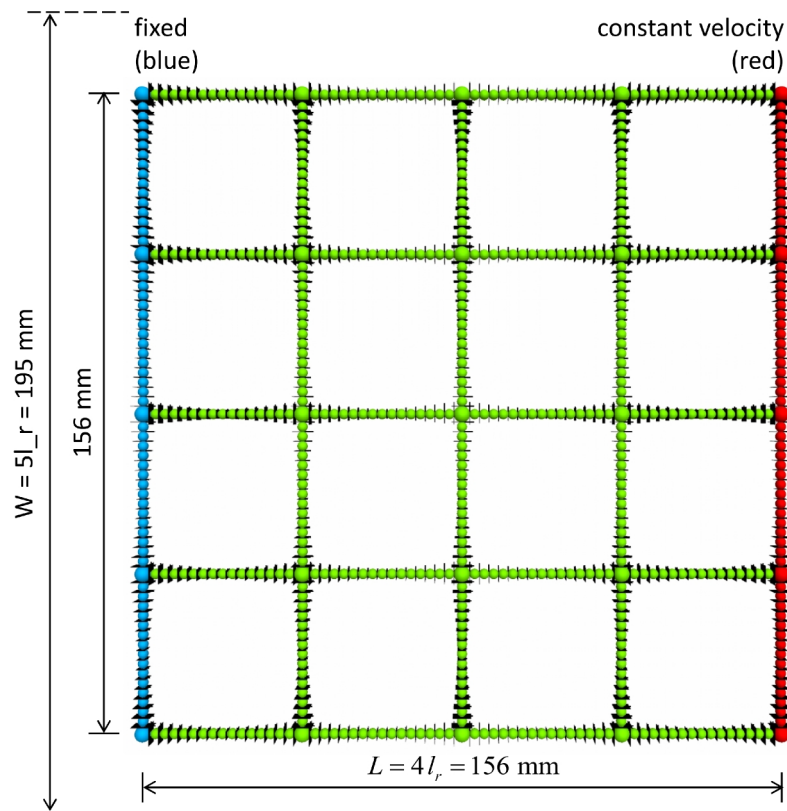


**Figure 29** The SS20 beamed grid showing the boundary conditions for the MAT test.

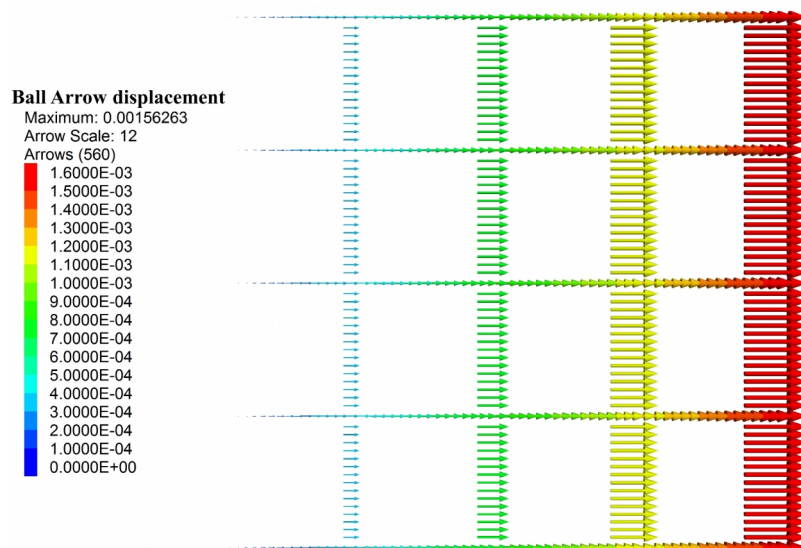


**Figure 30** The displacement field of the S20 beamed grid at the end of the MAT test after application of one-percent extension.



### 2.4.3 Beamed grid (triaxial)

The Tensar TX160 triaxial geogrid is modeled using the grid-set properties in Table 3. A grid section consisting of six by four apertures is clamped along its right and left edges as shown in Figure 31. The grid is subjected to a one-percent extension, and the displacement field is shown in Figure 32. The grid effective modulus is 62.3 MPa, which is 27% less than the average effective modulus of the biaxial grids. The triaxial grid also displays a Poisson effect, whereby the grid contracts in the lateral direction in response to extension in the axial direction. The Poisson effect is absent for the biaxial grids. The reduced effective modulus of the triaxial grid may be related to the Poisson effect.

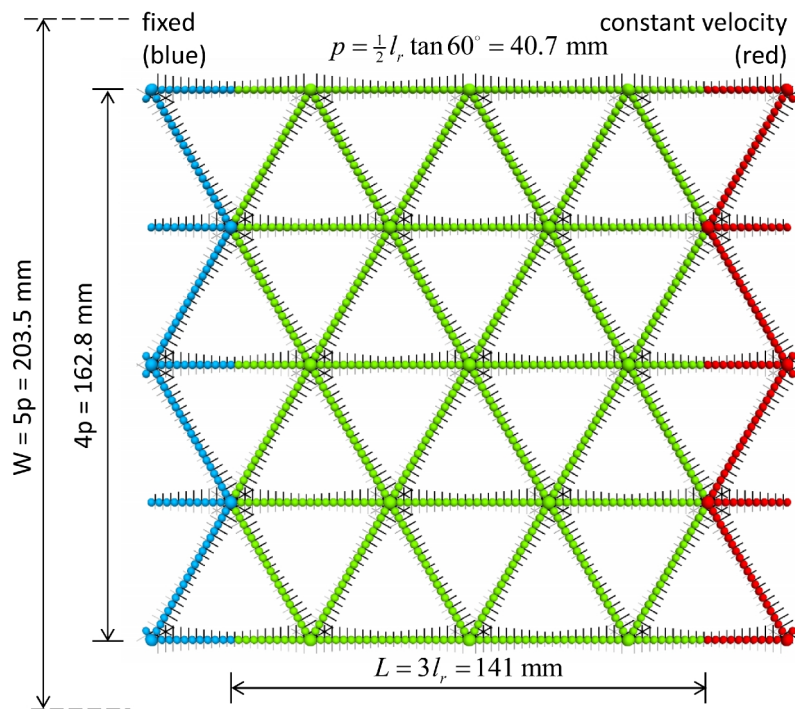


**Figure 31** The TX160 beamed grid showing the boundary conditions for the MAT test.

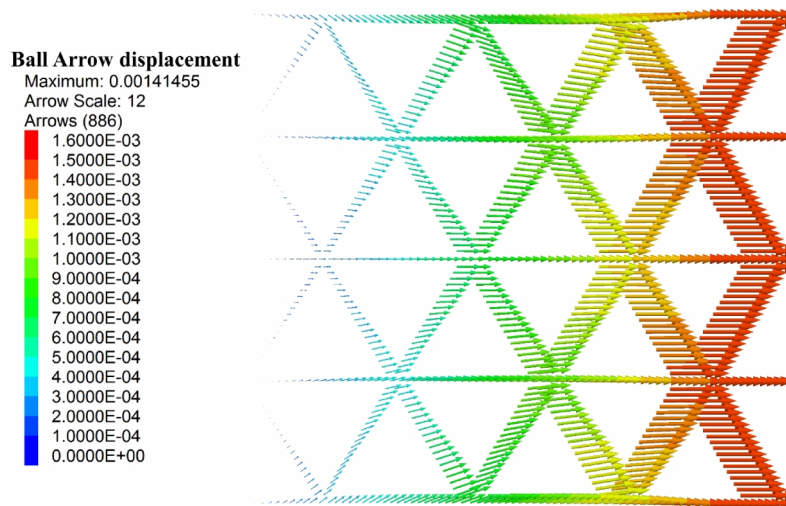


**Figure 32** *The displacement field of the TX160 beamed grid at the end of the MAT test after application of one-percent extension.*

## 2.5 Grid-Embedment Procedure

The material-genesis procedure of Potyondy (2019b) is modified to embed a geogrid in a granular material. The procedure occurs within a material vessel (in the form of either a polyaxial or cylindrical cell with frictionless walls) and produces a specimen consisting of a homogeneous, isotropic and well-connected grain assembly at a user-defined material pressure ( $P_m$ ) with an embedded and well-interlocked grid. The procedure consists of a packing phase followed by a finalization phase. During the packing phase, the grain assembly is subjected to the boundary-contraction packing procedure during which the friction coefficient is set to  $\mu_{CA}$  — typically chosen as zero to obtain a dense packing. During the finalization phase, the friction coefficient is set to its final value,  $\mu$ , which is assigned to existing grain-grain contacts and new grain-grain contacts that may form during subsequent motion.

The boundary-contraction packing procedure as modified to support grid embedment consists of the following five steps (see Figure 33).

1. Create the grid set in its initial, undeformed configuration within the material vessel, and constrain the grid by fixing the grid balls so that they cannot translate or rotate. The grid remains constrained during the next three steps, during which the grid does not move or deform while the grains flow around the grid.
2. Generate a cloud of grains with grain-cloud porosity of  $n_c$ . The grains are drawn from a specified size distribution, and then placed at arbitrarily chosen positions that lie fully within the material vessel and do not overlap an exclusion region that surrounds each grid. The exclusion region is a thin layer with a normal extent that just touches the node balls; and if

the lateral extent exists ( $C_e = 0$ ), then it just touches either the protruding half ribs or the outer node balls. There are large grain-grain overlaps in the grain cloud, but there are no grain-vessel or grain-grid overlaps. Typically,  $n_c$  is chosen equal to  $n_l$ , where  $n_l$  corresponds with the loose state for which grains are just in contact at a mean stress ( $\sigma_m$ ) of zero. For a fill material of nearly uniform-sized spheres and no embedded grid,  $n_l \cong 0.58$ , and this value must be decreased to obtain a material with an embedded grid that has the same number of grains as the material with no embedded grid.

3. Set the friction coefficient to zero, and then allow the grains to rearrange until either the mean stress is near zero or static equilibrium is obtained. This step eliminates the large grain-grain overlaps by allowing the grains to move apart and flow uniformly into the grid apertures from above and below. The material is in an isotropic state at the end of this step.
4. Set the material friction coefficient to  $\mu_{CA}$ , and then apply confinement by moving the vessel walls under control of a servomechanism until the wall pressures are within the specified tolerance of the material pressure and static equilibrium has been obtained. Setting  $\mu_{CA} = 0$  gives the densest packing, while progressively looser packings are obtained by increasing  $\mu_{CA}$ . Typically, one sets  $\mu_{CA} = 0$  to allow the grains to be compressed uniformly into the grid apertures, and thereby obtain a grid that is well-interlocked with the grain assembly.
5. Remove the grid constraint by freeing the grid balls so that they can translate and rotate. Repeat step 4 on the unconstrained grid to allow the grid to move and deform in response to the compressive forces imposed by the grains.

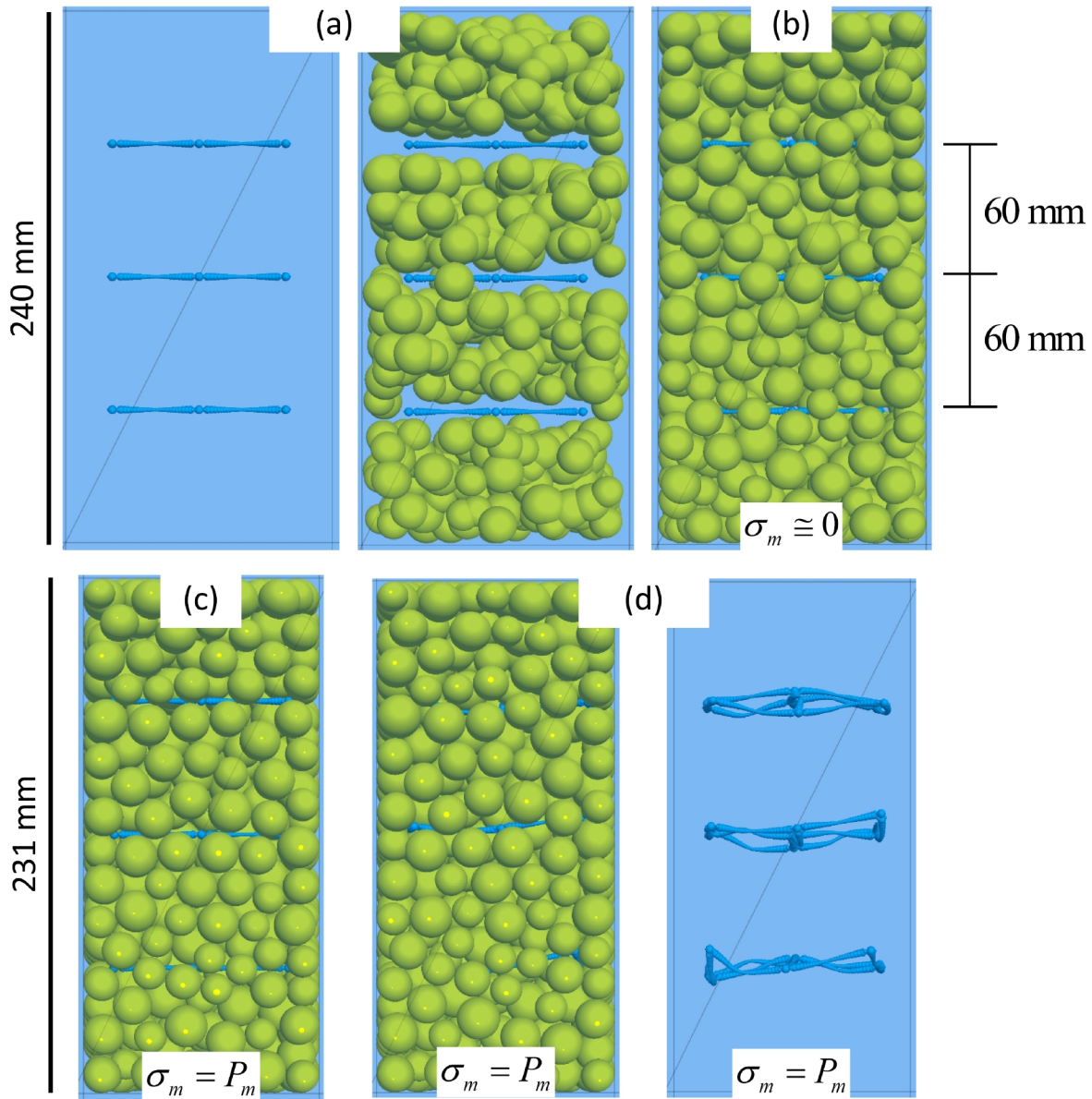


**Figure 33** *Grid-embedment procedure: (a) constrained grid and initial grain cloud at end of step 2, (b) constrained grid and relaxed grain cloud at end of step 3, (c) constrained grid and compacted granular assembly at end of step 4, and (d) unconstrained and deformed grid at end of step 5. The AG\_SS20 model of the simple pavement-design example is shown in non-perspective view.*

### 3.0 PAVEMENT-DESIGN EXAMPLES

There are two pavement-design examples described in this section. The AG example provides a base case at the lowest resolution sufficient to demonstrate system behavior, whereas the C5Q example provides a more realistic case.<sup>10</sup> The AG example models a cuboid with three 2 by 2 grids containing material with a narrow grain-size distribution subjected to simple boundary conditions. The C5Q example models a cuboid with one 6 by 6 grid containing material with a broad grain-size distribution that matches the upper end of the MnDOT Class 5Q material designation subjected to boundary conditions typical of an aggregate base layer.

#### 3.1 Simple Example

The simple pavement-design example is in the **MG-HillGrid** example-project directory. The example serves as a base case, and provides materials at the lowest resolution sufficient to demonstrate system behavior. Two instances of a hill material with a narrow grain-size distribution of grain diameters uniformly distributed from 14 to 20 mm are created.<sup>11</sup> The first instance is denoted as the AG material, and the second instance has three flat Tensar SS20 biaxial geogrids embedded within it (centered within the material vessel and oriented perpendicular to the specimen axis with a 60-mm spacing) and is denoted as the AG\_SS20 material (see Figures 34 to 36). The material microproperties are listed in Table 4, and the grid-set properties are listed in Table 5. The materials are dry while being created in a polyaxial material vessel (of initial 240-mm height and 120-mm width and depth, with a 500 MPa effective modulus) and packed at a 1 MPa material pressure as shown in Figure 34.

**Table 4 Microproperties of AG Materials\***

Property	Value
<b>Common group:</b>	
$N_m$	{AG, AG_SS20}
$\{T_m, N_{cm}\}, \alpha, C_p, \rho_v [\text{kg/m}^3]$	{4, hill}, 0.7, 0, 2650
$S_g, T_{SD}, \{D_{\{l,u\}} [\text{mm}], \phi\}, D_{mult}$	0, 0, {14, 20, 1.0}, 1.0
<b>Packing group:</b>	

<sup>10</sup> A more realistic example that has been developed based on the models described herein is in the “Typical Roadway Model” section of Potyondy (2018). The more realistic example is used to map out the modulus-porosity-grid-grain shape relationship.

<sup>11</sup> A hill material is defined as a granular assembly in which the hill contact model exists at all grain-grain contacts. The hill material behaves like an unsaturated granular material, and the grain-grain system behaves like two elastic spheres that may have a liquid bridge — refer to Potyondy (2019c) for a comprehensive description of the model.

$S_{RN}, P_m [\text{kPa}], \varepsilon_p, \varepsilon_{lim}, n_{lim}$	10000, 1000, $1 \times 10^{-2}$ , $8 \times 10^{-3}$ , $2 \times 10^6$
$C_p, n_c, \mu_{CA}, v_{lim} [\text{m/s}]$	0, {0.58, 0.427}, <sup>1</sup> 0, <sup>2</sup> 1.0
<b>Hill material group:</b>	
$E_g [\text{GPa}], \nu_g, \mu, \alpha_h, \psi [\text{kPa}]$	29, 0.15, 0.4, 0, 0

\* Hill material parameters are defined in Table 2 of Potyondy (2019c).

<sup>1</sup> The cloud porosity for the AG\_SS20 material is decreased so that this material has a similar number of grains as the AG material.

<sup>2</sup> The friction coefficient during confinement application is zero to obtain a dense packing.

**Table 5 Grid Set Properties of SS20 Parallel-Bonded Grids\***

Property	Value
<b>Grid set group:</b>	
$n_g, s_z [\text{mm}], \{n_x, n_y\}, c [\text{mm}], C_t$	$\left\{ \begin{aligned} &[3, 60.0, \{3, 3\}, (-39.0, -39.0, -60.0), 0], \text{ AG} \\ &[1, \text{NA}, \{6, 6\}, (-97.5, -97.5, 0), 0], \text{ C5} \end{aligned} \right\}$
$C_g, D_n [\text{mm}], l_r [\text{mm}], \kappa_r, n_c$	0, 4.0, 39.0, 0.9, 7
$\bar{R}_n [\text{mm}], \bar{R}_m [\text{mm}], \bar{\lambda}_j, C_e$	2.9, 1.0, 1.0, $\begin{cases} 0, & \text{AG} \\ 1, & \text{C5} \end{cases}$
<b>Material properties group:</b>	
$\alpha_g, \rho_g [\text{kg/m}^3], E_g^* [\text{MPa}], \kappa_g^*$	0.7, 950, 700, <sup>1</sup> 2.0
$E_{gs}^* [\text{MPa}], \kappa_{gs}^*, \mu_{gs}$	500, 2.0, 0.5

\* Grid-set parameters are defined in Table 1.

<sup>1</sup> SS20 properties in Stahl and te Kamp (2013) are 770 and 630 MPa in the TD and LD directions, respectively.

The aggregate properties are summarized as follows. There are approximately 550 granite grains modeled as spheres drawn from a narrow grain-size distribution, with grain diameters uniformly distributed from 14 to 20 mm. The grain density is  $2650 \text{ kg/m}^3$ . The Young's modulus and Poisson's ratio of the grains are 29 GPa and 0.15, respectively. The friction coefficient is 0.4. The suction is zero, because the material is dry. The damping constant is zero, because quasi-static conditions are enforced via local damping, with a local-damping factor of 0.7.

The grid material properties were taken from Stahl and te Kamp (2013). The grid density is  $950 \text{ kg/m}^3$ , which is similar to the  $946 \text{ kg/m}^3$  for polypropylene (Wikipedia, 2015a). The grid



effective modulus is 700 MPa, which is approximately one-half of the 1.5 – 2.0 GPa for polypropylene (Wikipedia, 2015b).<sup>12</sup> The grid stiffness ratio is two. The structural properties of the grid (quantified by the rib tensile stiffness and the junction torsional stiffness) match those of a Tensar SS20 biaxial geogrid. The material properties of the grid surface were chosen as follows. The grid-surface effective modulus should be large enough to prevent excessive grid-grain overlap, and the value was set equal to that of the material vessel. The grid-surface stiffness ratio was set equal to the grid stiffness ratio. The grid-surface friction coefficient was set to 0.5.

The two materials at the end of material genesis are shown in Figures 34 and 35, and the configuration of a grid layer is shown in Figure 36. Both materials have approximately 550 spherical grains, with grain diameters uniformly distributed from 14 to 20 mm. The 17.0 mm average grain diameter gives a vessel resolution (number of grains across the smallest vessel dimension) of 7.1. The AG\_SS20 material has a grid resolution (number of grains across a grid aperture) of 2.3. Both materials are dry, packed at a 1.0 MPa material pressure, and have a porosity of 0.379. Both materials have approximately the same number of dry hill contacts (1362 and 1328 for the AG and AG\_SS20 materials, respectively), while the AG\_SS20 material has an additional 2388 internal grid contacts and 421 grid-grain contacts. The internal grid contacts join the 1143 grid balls to one another via parallel bonds (denoted as grid bonds in Figure 36).

We confirm that the materials form well-connected grain assemblies at the 1 MPa material pressure by plotting the mean stress and noting that the measurement-based value has reached the wall-based value, which is equal to the 1 MPa material pressure (see Figure 37). The material with the embedded grid requires more cycles to achieve this state, and the measurement-based mean stress lags behind the wall-based value.

---

<sup>12</sup> Our value is approximately one-half that of the physical material because of the extensive parallel-bond overlinking, whereby as one proceeds along a rib, each rib ball is joined to the next two rib balls. The overlinking is removed by removing the mid-rib and tip-rib balls, and the structural properties of such a grid match those of a Tensar SS20 biaxial geogrid by setting the grid effective modulus to 1.7 GPa.



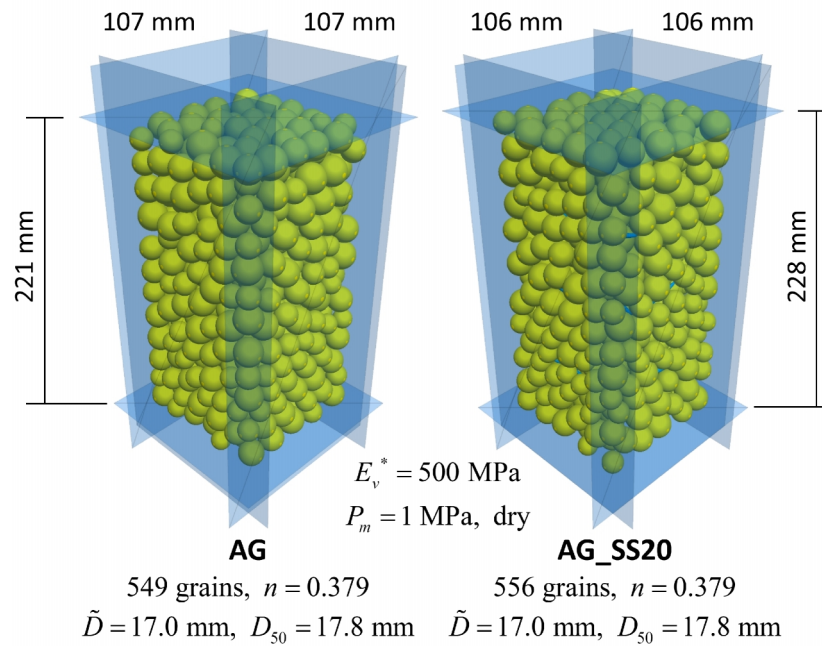


**Figure 34** Dry AG and AG\_SS20 materials at the end of material genesis.

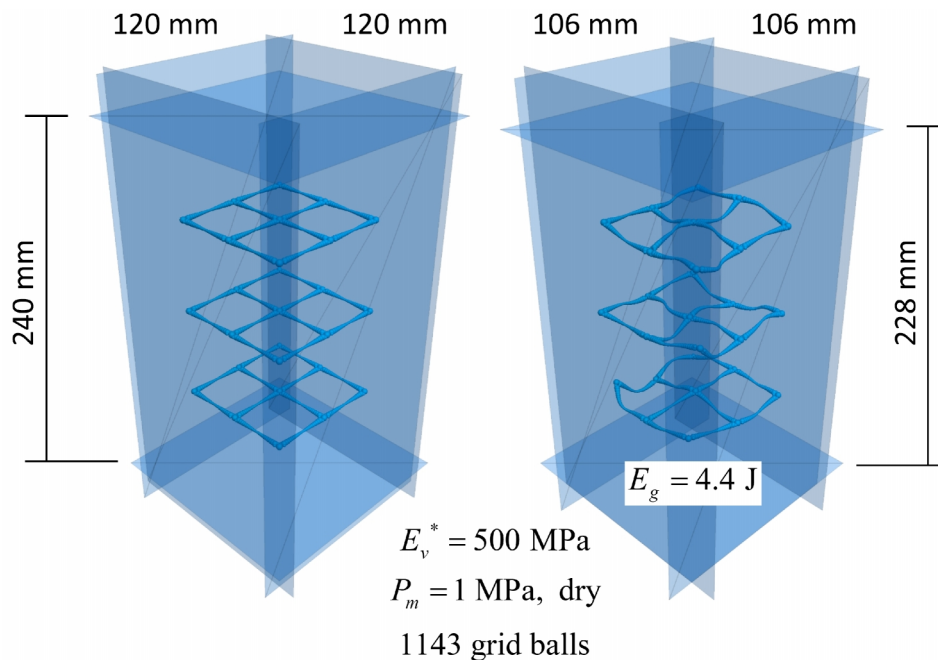


**Figure 35** The embedded grid set in the AG\_SS20 material in the polyaxial vessel at the start (left image) and end (right image) of material genesis.

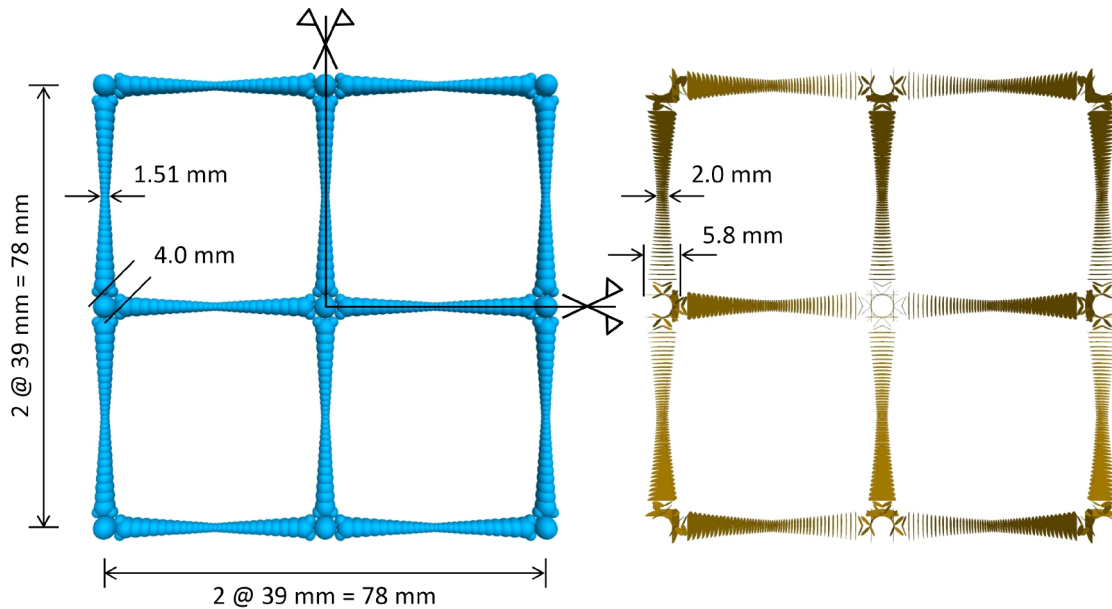


**Figure 36** The undeformed configuration of a grid layer in the AG\_SS20 material showing grid balls (left image) and grid bonds (right image).

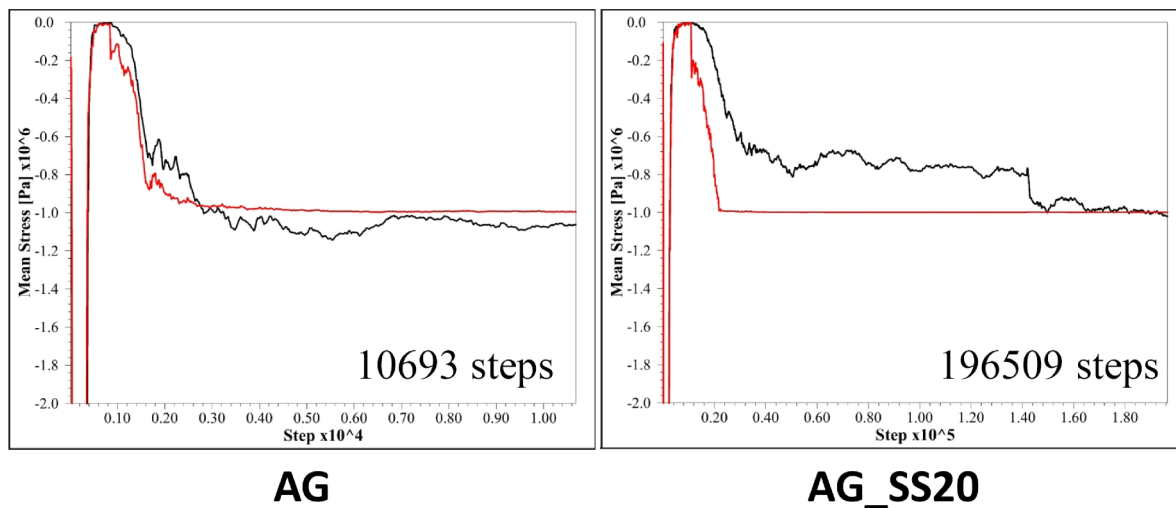


**Figure 37** Mean stress acting on the boundary (red) and within the material (black) versus step for the AG and AG\_SS20 materials during material genesis.

The macroscopically applied compressive load is carried by the granular material as force chains that propagate from one grain to the next across grain-grain contacts. The force-chain fabric is depicted as a network of cylinders, with a cylinder at each contact. Force magnitude corresponds with cylinder thickness and color, and force direction corresponds with cylinder orientation. An examination of the force-chain fabric at the end of material genesis reveals the following material characteristics. Both materials have a similar force-chain fabric, with maximum forces of approximately 2000 N (see Figure 38). The middle grid in the AG\_SS20 material is being compressed by the grains with a maximum force of 250 N, and its front-most aperture is being loaded in tension (see Figure 39). The compressive forces acting on the grids cause them to deform, and the total strain energy stored in the three grids is 4.4 Joules (see Figure 35). If the grains were removed, and the model cycled to a new state of static equilibrium, the grids would return to their undeformed configurations.

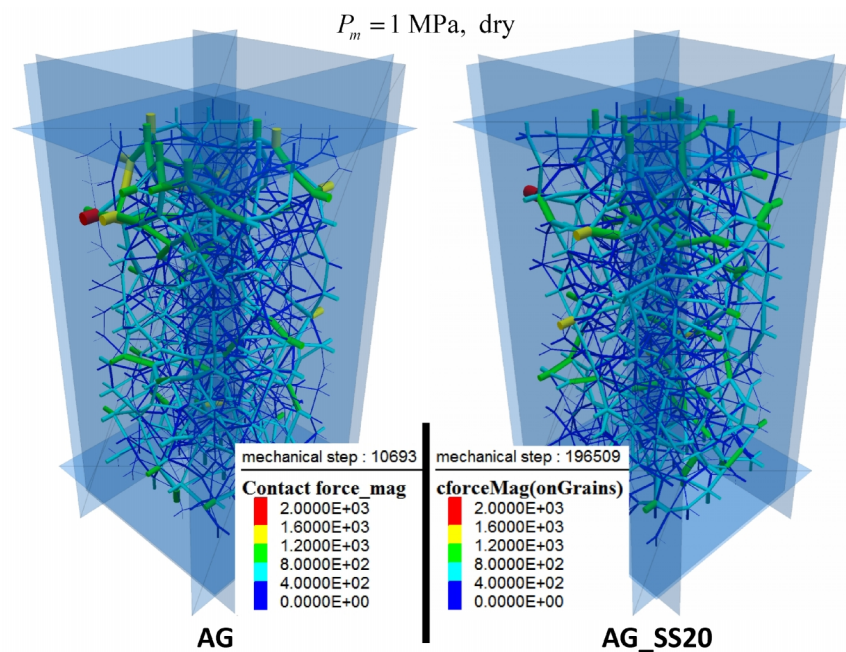


**Figure 38** *Force-chain fabric in the AG and AG\_SS20 materials in the polyaxial vessel at the end of material genesis.*

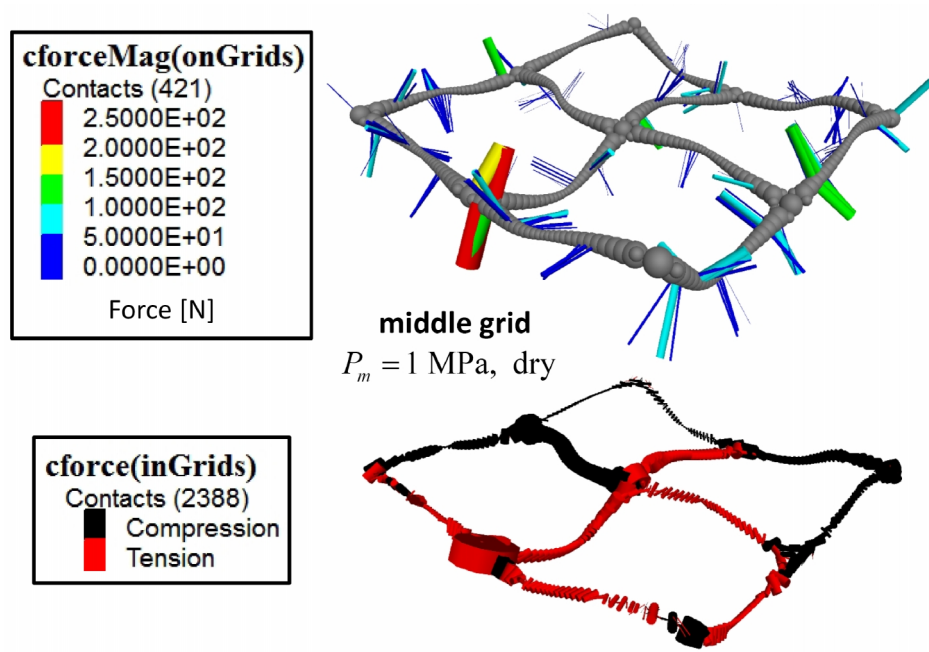


**Figure 39** Forces acting on and in the middle grid in the AG\_SS20 material in the polyaxial vessel at the end of material genesis.

The AG materials are subjected to triaxial testing. The materials are tested dry and wet. The wet material has a 20 kPa suction added between all grains that are within 3 mm of one another at the end of material genesis. During each triaxial test, the confinement is 1 MPa, and a load-unload cycle is performed at an axial strain of one percent to produce the deformation fields shown in Figure 40, and the stress-strain curves in Figures 41 and 42. The response is hysteretic. The grid and moisture both increase the material strength (measured as the deviator stress at one percent axial strain). The grid delays the onset of material dilation. The resilient modulus of the dry AG material with no grid is measured as 239 MPa in Figure 43, and the resilient moduli for the other cases are similar. The grid has a negligible effect on the resilient modulus of this simple system, but the grid increases the resilient modulus of the more realistic system examined in the next section.<sup>13</sup>

<sup>13</sup> A demonstration of the confining effect of the grid could be obtained by performing a cyclic triaxial test similar to the one described in Section 3.2 of McDowell et al. (2006), and examining the force chains after partial unloading. The cyclic triaxial test has 10-kPa confinement. Deviator stress is cycled 10–20 kPa (3 times), 10–30 kPa (three times), and then 10–40 kPa (three times). The partial unloading consists of reducing the confinement to 5 kPa.

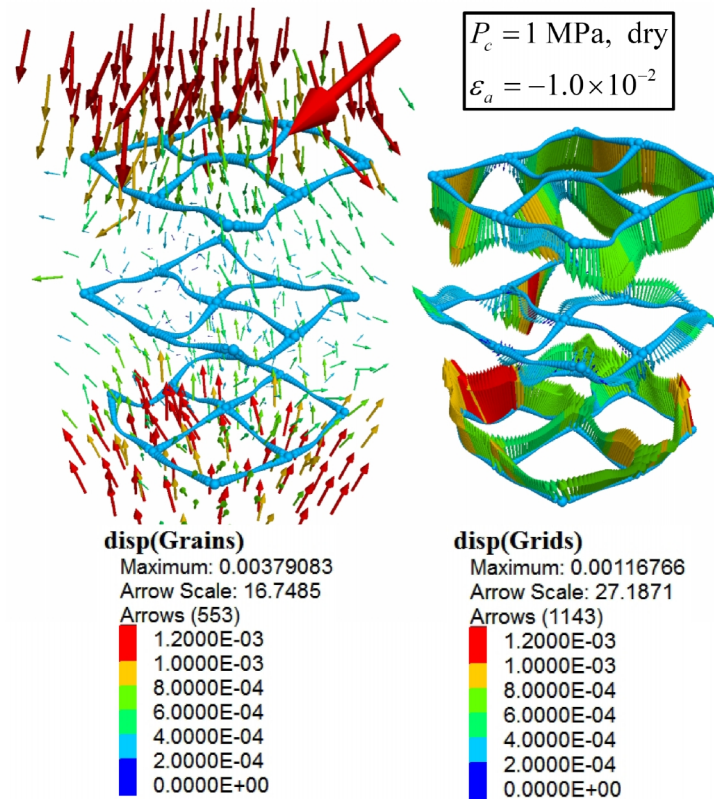


**Figure 40** Displacement fields of the dry AG\_SS20 material (left) and grid (right) after application of one percent axial strain. The top and bottom grids flow with the material and move toward one another. There is very little radial expansion to be resisted by the grids. The walls of the polyaxial vessel are not shown in these images.

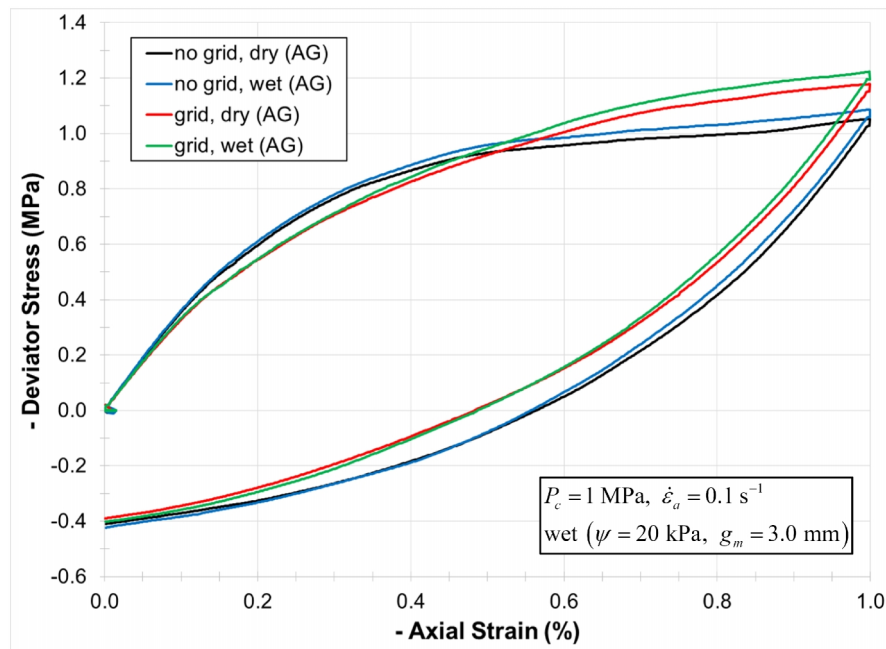


**Figure 41** Deviator stress versus axial strain for dry and wet AG and AG\_SS20 materials tested at 1 MPa confinement.

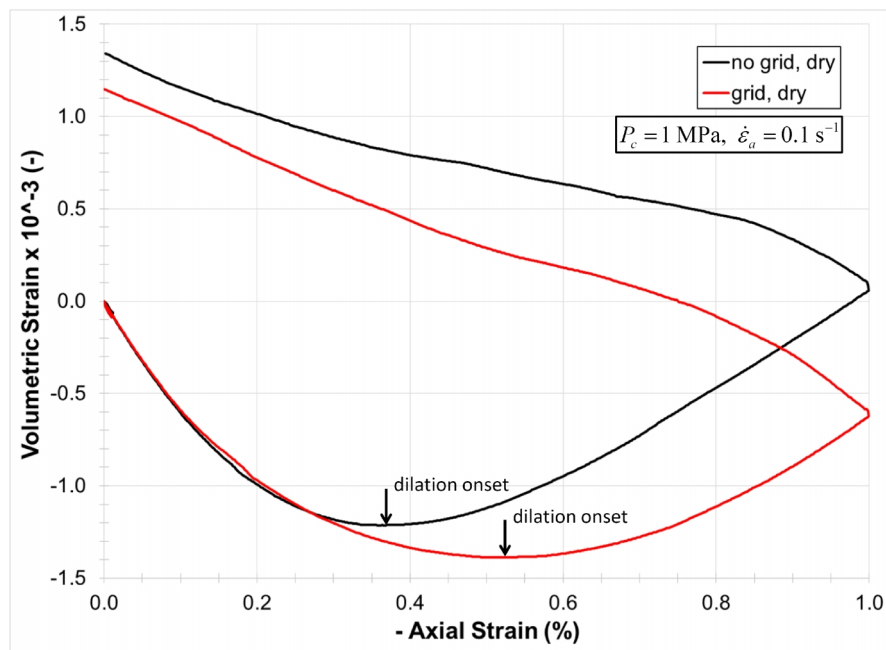


**Figure 42** Volumetric strain versus axial strain for dry AG and AG\_SS20 materials tested at 1 MPa confinement, and dilation onset.



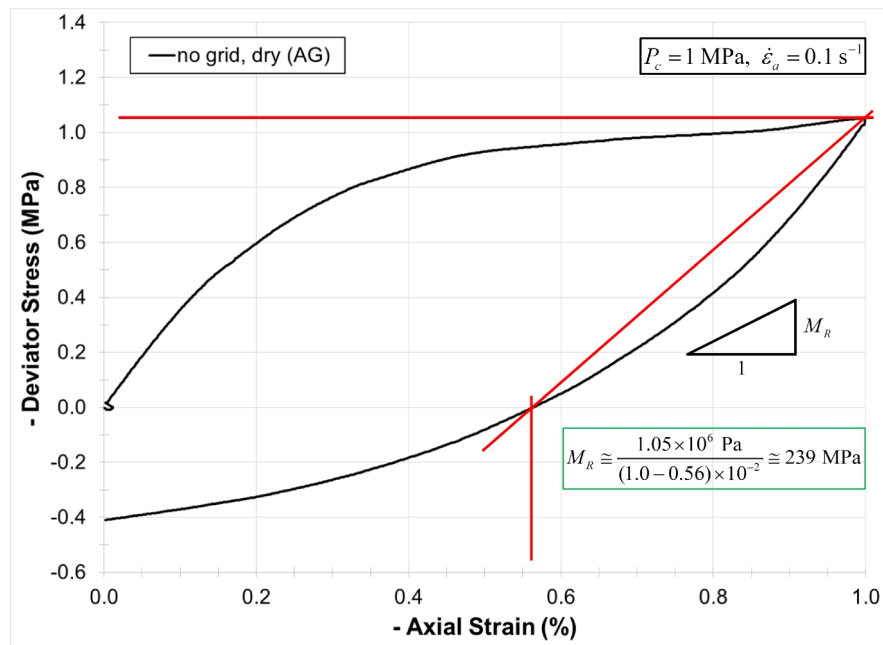


**Figure 43** *Deviator stress versus axial strain for dry AG material tested at 1 MPa confinement, and resilient modulus.*

### 3.2 Realistic Example

The realistic pavement-design example is in the **MatGen-HillGrid\_C5Q** example-project directory. Two instances of a hill material are created to represent the aggregate base layer of an asphalt-surface roadway (Potyondy et al., 2016; Siekmeier et al., 2016). The grain-size distribution lies within the upper end of the MnDOT Class 5Q aggregate base grading designation (see Figure 44). The first instance is denoted as the C5Q material, and the second instance has one flat Tensar SS20 biaxial geogrid embedded within it (centered within the material vessel and oriented perpendicular to the specimen axis) and is denoted as the C5Q\_SS20 material (see Figure 45).

The C5Q materials are subjected to triaxial testing. The materials are tested dry and moist. The moist material has a 30 kPa suction added between all grains that are within 3 mm of one another at the end of material genesis.<sup>14</sup> During each triaxial test, the confinement is 150 kPa, and a load-unload cycle is performed at an axial strain of 0.02% to measure the resilient moduli of the dry and moist materials (see Figure 46).<sup>15</sup>

<sup>14</sup> The suction is typical for aggregates with gravimetric moisture content ranging from 5 to 10 percent.

<sup>15</sup> The confinement is similar to that defined in resilient modulus laboratory protocols, and axial strains correspond with vertical strains in the aggregate base layer for typical traffic loads.



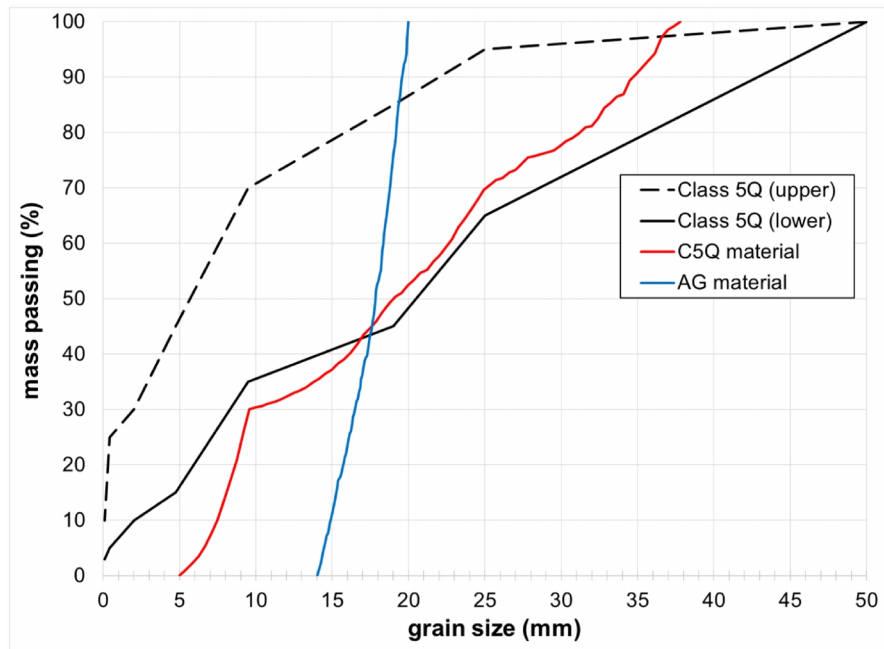


**Figure 44** Grain size distribution curves for the C5Q and AG materials along with the limits of the MnDOT Class 5Q aggregate base grading designation. (Class 5Q limits from MnDOT (2016), Table 3138-3: Base and Surfacing Aggregate [containing less than 25 percent recycled aggregates].)

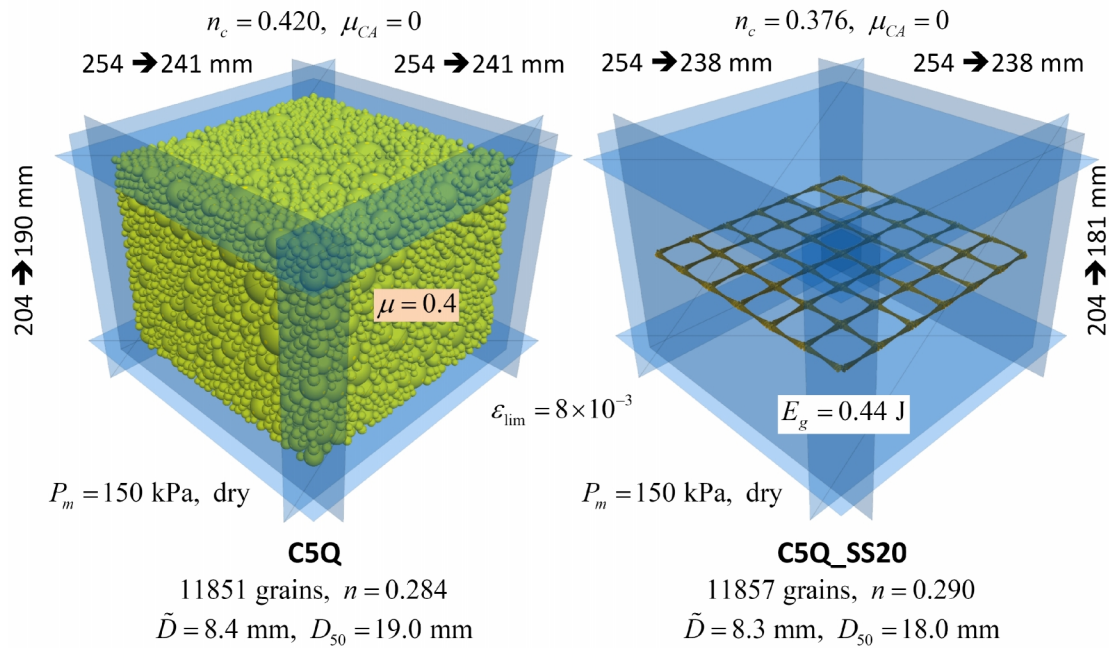


**Figure 45** C5Q material and embedded grid set in the C5Q\_SS20 material at the end of material genesis.

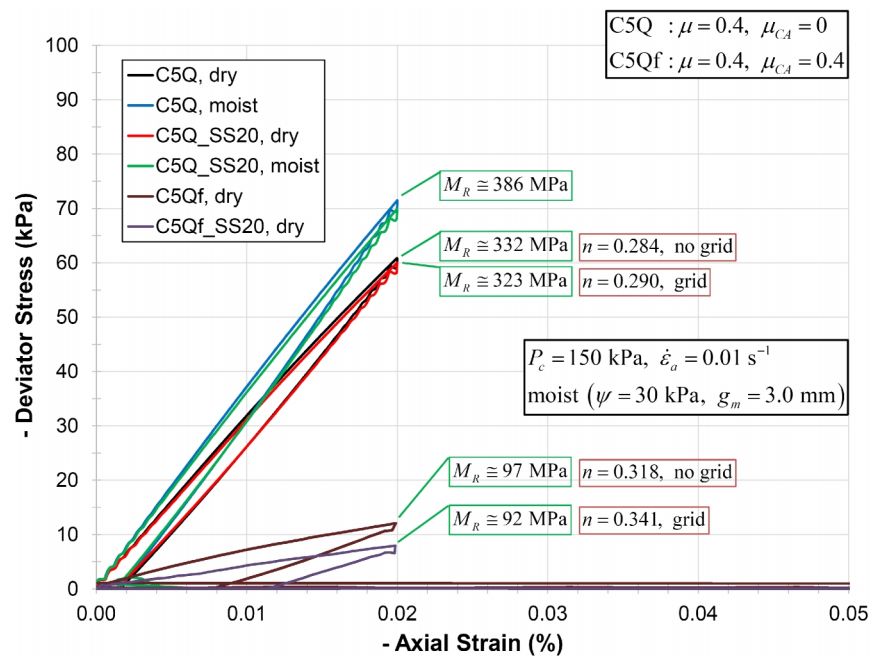


**Figure 46** Deviator stress versus axial strain for dry and moist C5Q and C5Q\_SS20 materials tested at 150 kPa confinement.

Adding moisture stiffens the material for both the no-grid and grid cases (increasing the resilient modulus from approximately 332 MPa to 386 MPa); however, the material stiffness is the same for the no-grid and grid cases. Why is this, and is this a general conclusion? Additional study has demonstrated that there is a general relationship between resilient modulus and material porosity, with resilient modulus decreasing as porosity increases from 0.28 to 0.35. By varying  $\mu_{CA}$  from zero to the true material friction coefficient, two distinct curves are obtained, one for the no-grid model and the other for the grid model, with the no-grid curve lying beneath the grid curve (see Figure 47).<sup>16</sup> When  $\mu_{CA}$  is non-zero, the material porosity of the no-grid specimen is less than that of the grid specimen. We speculate that the grid is inhibiting the packing process, forming a local region that is more porous than the surrounding region, and thereby increasing the overall material porosity.<sup>17</sup> The porosities of 0.284 and 0.290 for the case shown in Figure 46 are the lowest porosities that one can obtain for this material, because the friction coefficient has been set to zero ( $\mu_{CA} = 0$ ) during packing. For this case, the resilient moduli for the no-grid and grid models are approximately equal. The effect of the grid on material stiffness is found by comparing the resilient moduli for the no-grid and grid cases at the same material porosity. When this is done, we find that the presence of the grid increases the resilient modulus by factors ranging from 1.0 to approximately 2.5 depending on confinement and moisture conditions.

---

<sup>16</sup> The material shown in Figure 47 has a true material friction coefficient of 0.6. The porosity varies from the use of different friction coefficients during packing. The gain factor for a porosity of 0.323 is 1.8.

<sup>17</sup> The material porosity is obtained as the average value from three spherical measurement regions placed symmetrically along the axis of the largest vessel dimension (see section “Stress, Strain and Porosity in the Material” in Potyondy [2017a]).

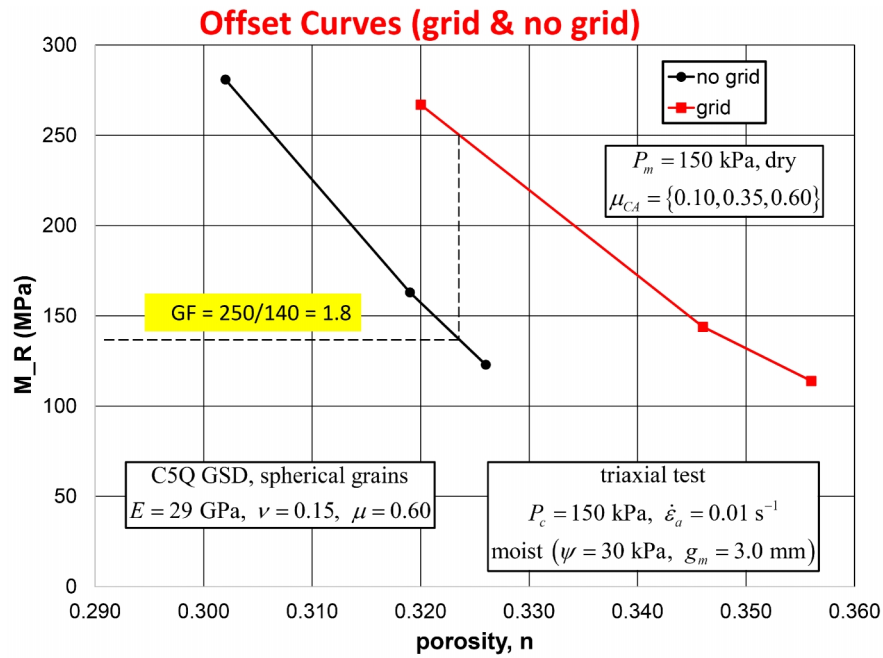


**Figure 47** Resilient modulus versus porosity for grid and no-grid models with friction coefficients during packing varying from 0.1 to 0.6, and tested moist at 150 kPa confinement.

## 4.0 REFERENCES

- Bagshaw, S.A., P.R. Herrington, P. Kathirgamanathan and S.R. Cook. (2015) “Geosynthetics in Basecourse Reinforcement,” Opus International Consultants Ltd., Report to NZ Transport Agency, Wellington, New Zealand, NZ Transport Agency Research Report 574, September 2015.
- Buchanan, S. (2007) “Resilient Modulus: What, Why, and How?” Vulcan Materials Company, August 31, 2007. Document **2-Resilient-Modulus-Buchanan.pdf** accessed from [www.vulcaninnovations.com/public/pdf](http://www.vulcaninnovations.com/public/pdf) on November 6, 2015
- Chen, C., G.R. McDowell and N.H. Thom. (2013) “A Study of Geogrid-Reinforced Ballast using Laboratory Pull-Out Tests and Discrete Element Modelling,” *Geomechanics and Geoengineering*, **8**(4), 244–253.
- Clyne, T. (2001) “Monitoring Geosynthetics in Local Roadways 10-Year Performance Summary,” Minnesota Department of Transportation, Saint Paul, MN, 2001.
- Cook, R.D., D.S. Malkus and M.E. Plesha. (1989) *Concepts and Applications of Finite Element Analysis*, Third Edition, New York: John Wiley & Sons.
- Crandall, S.H., N.C. Dahl and T.J. Lardner. (1978) *An Introduction to the Mechanics of Solids*, Second Edition, New York: McGraw-Hill Book Company.
- Han, Z., and S.K. Vanapalli. (2016) “State-of-the-Art: Prediction of Resilient Modulus of Unsaturated Subgrade Soils,” *Int. J. Geomechanics*, 10.1061/(ASCE)GM.1943-5622.0000631, 04015104.
- Itasca Consulting Group, Inc. (2019) *PFC — Particle Flow Code in 2 and 3 Dimensions*, Version 6.0, Documentation Set of version 6.00.12 [April 7, 2019]. Minneapolis: Itasca.
- Jas. H., M. Stahl, H. Konietzky, L. te Kamp and T. Oliver. (2015a) “Discrete Element Simulation of Geogrid Stabilized Sub-Base: Modelling and Calibration and Plate Load Simulation under Special Consideration of Important Boundary Conditions,” to appear in *Sixth Symposium on Deformation Characteristics of Geomaterials* (Buenos Aires, Argentina, November 2015).
- Jas. H., M. Stahl, H. Konietzky, L. te Kamp and T. Oliver. (2015b) “Discrete Element Modeling of a Trafficked Sub-Base Stabilized with Biaxial and Multi-Axial Geogrids to Compare Stabilization Mechanisms,” *Proc. Geosynthetics 2015* (Portland, OR, February 15–18, 2015), pp. 245–254.
- Konietzky, H., L. te Kamp, T. Groeger and C. Jenner. (2004) “Use of DEM to Model the Interlocking Effect of Geogrids under Static and Cyclic Loading,” *Numerical Modeling in*

*Micromechanics via Particle Methods*, pp. 3–11, Y. Shimizu, R. Hart and P. Cundall, Eds., Taylor & Francis Group, London.

McDowell, G.R., O. Harireche, M. Konietzky, S.F. Brown and N.H. Thom. (2006) “Discrete Element Modelling of Geogrid-Reinforced Aggregates,” *Proceeding of the Institution of Civil Engineers — Geotechnical Engineering*, **159**(1), 35–48.

MnDOT. (2016) *Standard Specifications for Construction*, 2016 Edition, Minnesota Dept. of Transportation, Saint Paul, MN.

Potyondy, D. (2019a) “Beam Contact Model [version 1],” Itasca Consulting Group, Inc., Technical Memorandum 2-3558-01:17TM07 (April 17, 2019), Minneapolis, Minnesota.

Potyondy, D. (2019b) “Material-Modeling Support in PFC [fistPkg6.5],” Itasca Consulting Group, Inc., Technical Memorandum ICG7766-L (April 5, 2019), Minneapolis, Minnesota.

Potyondy, D. (2019c) “Hill Contact Model [version 4],” Itasca Consulting Group, Inc., Technical Memorandum ICG7795-L (April 5, 2019), Minneapolis, Minnesota.

Potyondy, D. (2018) “Model-Validation Tests,” Itasca Consulting Group, Inc., Technical Memorandum 2-3558-01:17TM52 (June 22, 2018), Minneapolis, Minnesota.

Potyondy, D. O. (2015) “The Bonded-Particle Model as a Tool for Rock Mechanics Research and Application: Current Trends and Future Directions,” *Geosystem Engineering*, **18**(1), 1–28.

Potyondy, D., J. Siekmeier and L. Petersen. (2016) “Aggregate-Geogrid Interaction Model Incorporating Moisture Effects,” in Transportation Research Board 2016 Annual Meeting Compendium of Papers.

Qian, Y., D. Mishra, E. Tutumluer and H.A. Kazmee. (2015) “Characterization of Geogrid Reinforced Ballast Behavior at Different Levels of Degradation through Triaxial Shear Strength Test and Discrete Element Modeling,” *Geotextiles and Geomembranes*, **43**(5), 393–402.

Siekmeier, J., and J. Casanova. (2016) “Geogrid Reinforced Aggregate Base Stiffness for Mechanistic Pavement Design,” Saint Paul, Minnesota, Minnesota Department of Transportation Research Report 2016-24, MN/RC 2016-24, July 2016.

Siekmeier, J., J. Bittmann, D. Potyondy and L. Petersen. (2016) “Introducing a Geogrid Gain Factor for Flexible Pavement Design,” in *Proceedings University of Minnesota 64th Annual Geotechnical Engineering Conference* (Saint Paul, MN, March 4, 2016).

Skallman, J. (2010) “Geogrids (Multiaxial) on CSAH and MSAS Routes — General Specification, Granular Equivalent (G.E.) and Design Guidelines,” Minnesota Dept. of Transportation, Saint Paul, MN, Tech. Memo. 10-SA-03, December 21, 2010.

Stahl, M. (2011) “Interaktion Geogitter-Boden: Numerische Simulation und Experimentelle Analyse,” Ph.D. Thesis, Technische Universität Bergakademie Freiberg, Germany, Heft 2011-5 (in German).

Stahl, M., and H. Konietzky. (2011) “Discrete Element Simulation of Ballast and Gravel under Special Consideration of Grain-Shape, Grain-Size and Relative Density,” *Granular Matter*, **13**, 417–428.

Stahl, M., H. Konietzky, L. te Kamp and H. Jas. (2014) “Discrete Element Simulation of Geogrid-Stabilised Soil,” *Acta Geotechnica*, **9**, 1073–1084.

Stahl, M., and L. te Kamp. (2013) “Project 13008: Geogrid Modelling with PFC3D — Generation and Calibration of Biaxial Geogrid SS20,” Itasca Consultants GmbH, Gelsenkirchen, Germany, Report to Tensar International Ltd., United Kingdom, Report 01-2013, February 20, 2013.

Stahl, M., and L. te Kamp. (2012) “Project 12206: Geogrid Modelling with PFC3D — Generation and Calibration of TriAx-Geogrid TX160,” Itasca Consultants GmbH, Gelsenkirchen, Germany, Report to Tensar International Ltd., United Kingdom, Report 01-2012, September 26, 2012.

Stille, B. (2015) “Geogrid Modeling Package,” PowerPoint slide sets: **TensarSS20-Generate&Calibrate.ppt** and **GeogridPackage.pptx**.

Tanquist, B. (2012) *MnPAVE User's Guide*. Office of Materials, Minnesota Dept. of Transportation, Maplewood, MN, July 2012.

Wikipedia. (2015a) Entry for “density polypropylene” on June 4, 2015.

Wikipedia. (2015b) Entry for “young's modulus polypropylene” on June 4, 2015.